

1    2 **TITLE:**

2    4 Phosphorylation barcodes direct biased chemokine signaling at CXCR3

3    6

4    9 **AUTHORS:**

5    10

6    11 Dylan S. Eiger<sup>1,†</sup>, Jeffrey S. Smith<sup>2-6,†</sup>, Tujin Shi<sup>7</sup>, Tomasz Maciej Stepniewski<sup>8</sup>, Chia-Feng Tsai<sup>7</sup>, Christopher

7    12 Honeycutt<sup>9</sup>, Noelia Boldizsar<sup>9</sup>, Julia Gardner<sup>9</sup>, Carrie D. Nicora<sup>7</sup>, Ahmed M. Moghieb<sup>10</sup>, Kouki Kawakami<sup>11</sup>, Issac

8    13 Choi<sup>12</sup>, Kevin Zheng<sup>9</sup>, Anmol Warman<sup>9</sup>, Priya Alagesan<sup>1</sup>, Nicole M. Knape<sup>1</sup>, Ouwen Huang<sup>13</sup>, Justin D.

9    14 Silverman<sup>14</sup>, Richard D. Smith<sup>7</sup>, Asuka Inoue<sup>11</sup>, Jana Selent<sup>8</sup>, Jon M. Jacobs<sup>7</sup>, Sudarshan Rajagopal<sup>1,11,\*</sup>,

10    15

11    16

12    17

13    18

14    19

15    20

16    21

17    22 † = these authors contributed equally

18    23

19    24 \* = corresponding author

20    25

21    26 <sup>o</sup> = lead contact

22    27

23    28

24    29

25    30

26    31

27    32

28    33

29    34

30    35

31    36

32    37

33    38

34    39

35    40

36    41

37    42

38    43

39    44

40    45

41    46

42    47

43    48

44    49

45    50

46    51

47    52

48    53

49    54

50    55

51    56

52    57

53    58

54    59

55    60

56    61

57    62

58    63

59    64

60    65

## AFFILIATIONS:

<sup>1</sup>Department of Biochemistry, Duke University, Durham, NC, 27710, USA

<sup>2</sup>Department of Dermatology, Massachusetts General Hospital, Boston, MA, 02114, USA

<sup>3</sup>Department of Dermatology, Brigham and Women's Hospital, Boston, MA, 02115, USA

<sup>4</sup>Department of Dermatology, Beth Israel Deaconess Medical Center, Boston, MA, 02215, USA

<sup>5</sup>Dermatology Program, Boston Children's Hospital, Boston, MA, 02115, USA

<sup>6</sup>Harvard Medical School, Boston, MA 02115 USA

<sup>7</sup>Biological Sciences Division, Pacific Northwest National Laboratory, Richland, WA 99354, USA

<sup>a</sup>Research Programme on Biomedical Informatics (CRIB), Department of Experimental and Health Sciences of the University of Valencia.

Université de Montréal (UdeM) - Institut des mathématiques et de la statistique (IMSM) - Bureau 6260 - 3650 Côte-Sainte-Catherine

<sup>9</sup>Trinity College, Duke University, Durham, NC 27710, USA

<sup>10</sup>R&D Research, GlaxoSmithKline, Collegeville, PA 19426, USA

<sup>11</sup>Department of Pharmaceutical Sciences, Tohoku University, Sendai, 980-8577, Japan.

<sup>12</sup>Department of Medicine, Duke University, Durham, NC 27710 USA

## CORRESPONDENCE

sudarshan.raiagopal@duke.edu

1  
34 2 **SUMMARY**  
3

4 G protein-coupled receptor (GPCR) biased agonism, the activation of some signaling pathways over  
5 others, is thought to largely be due to differential receptor phosphorylation, or “phosphorylation barcodes.” At  
6  
7 chemokine receptors, ligands act as “biased agonists” with complex signaling profiles, which contributes to the  
8  
9 limited success in pharmacologically targeting these receptors. Here, mass spectrometry-based global  
10 phosphoproteomics revealed that CXCR3 chemokines generate different phosphorylation barcodes associated  
11 with differential transducer activation. Chemokine stimulation resulted in distinct changes throughout the kinome  
12  
13 in global phosphoproteomic studies. Mutation of CXCR3 phosphosites altered β-arrestin conformation in cellular  
14 assays and was confirmed by molecular dynamics simulations. T cells expressing phosphorylation-deficient  
15 CXCR3 mutants resulted in agonist- and receptor-specific chemotactic profiles. Our results demonstrate that  
16 CXCR3 chemokines are non-redundant and act as biased agonists through differential encoding of  
17 phosphorylation barcodes and lead to distinct physiological processes.  
18  
19  
20  
21  
22  
23  
24  
25  
26  
27  
28  
29  
30  
31  
32  
33  
34  
35  
36  
37  
38  
39  
40  
41  
42  
43  
44  
45  
46  
47  
48  
49  
50  
51  
52  
53  
54  
55  
56  
57  
58  
59  
60  
61  
62  
63  
64  
65

1  
2 **KEYWORDS:** *beta-arrestin, G protein-coupled receptor, biased agonism, chemokine, CXCR3,*  
3  
4 *phosphoproteomics, chemotaxis, MAP kinase, mass spectrometry, molecular dynamics*  
5  
6  
7  
8  
9  
10  
11  
12  
13  
14  
15  
16  
17  
18  
19  
20  
21  
22  
23  
24  
25  
26  
27  
28  
29  
30  
31  
32  
33  
34  
35  
36  
37  
38  
39  
40  
41  
42  
43  
44  
45  
46  
47  
48  
49  
50  
51  
52  
53  
54  
55  
56  
57  
58  
59  
60  
61  
62  
63  
64  
65

1  
48 **INTRODUCTION**  
2  
3

4 G protein-coupled receptors (GPCRs) are the most common transmembrane receptors in the human  
5 genome and the target of approximately one third of all FDA-approved drugs (Hauser et al., 2017). GPCRs elicit  
6 cellular responses by coupling to heterotrimeric G proteins, recruiting GPCR kinases (GRKs), and binding to β-  
7 arrestin adaptor proteins (Smith and Rajagopal, 2016). Certain GPCR ligands can promote or inhibit different  
8 GPCR conformational states, leading to distinct G protein or β-arrestin signaling outputs; i.e. display “biased  
9 agonism”. Efforts are underway to design biased agonists that preferentially activate certain signaling pathways  
10 to maximize clinical efficacy and reduce off-target effects (Pupo et al., 2016). However, the molecular  
11 determinants of biased signaling and the degree to which different ligands can modulate intracellular signaling  
12 cascades remain unclear.  
13  
14

15 Altering intracellular GPCR amino acid residue phosphorylation patterns can lead to different signaling  
16 events and is one mechanism for encoding biased agonism (Busillo et al., 2010; Butcher et al., 2011; Dwivedi-  
17 Agnihotri et al., 2020; Latorraca et al., 2020; Nobles et al., 2011). For example, preventing phosphorylation of  
18 certain residues impairs receptor endocytosis but not β-arrestin recruitment (Oakley et al., 1999). Specific GPCR  
19 phosphorylation patterns also differentially alter the affinity of GPCR-β-arrestin interactions (Bouzo-Lorenzo et  
20 al., 2016; Jung et al., 2017; Lee et al., 2016; Mayer et al., 2019; Sente et al., 2018). GPCR agonists are thought  
21 to regulate β-arrestin function by encoding distinct phosphorylation events through selective interaction with  
22 different GRKs (Busillo et al., 2010; Butcher et al., 2011; Inagaki et al., 2015; Komolov and Benovic, 2018; Nobles  
23 et al., 2011). This “phosphorylation barcode hypothesis” is supported by mutagenesis studies in both cellular  
24 and animal models (Bradley et al., 2020; Kaya et al., 2020; Kliewer et al., 2019; Mann et al., 2020; Marsango et  
25 al., 2022; Scarpa et al., 2021; Zhou et al., 2017). Biophysical data also support that different C-terminal  
26 phosphorylation patterns induce distinct β-arrestin conformational states (Dwivedi-Agnihotri et al., 2020; Lee et  
27 al., 2016; Mayer et al., 2019; Nobles et al., 2011; Nuber et al., 2016; Yang et al., 2015; Yang et al., 2017), and  
28 may expose β-arrestin binding sites for some downstream effectors but not others (Latorraca et al., 2020).  
29 However, it is unclear if different C-terminal residues are phosphorylated or if the same residues are  
30 phosphorylated at differing stoichiometric ratios, a distinction critical to understanding how GPCR is  
31 mechanistically encoded. In addition, few studies have identified distinct phosphopeptides or associated changes  
32  
33  
34  
35  
36  
37  
38  
39  
40  
41  
42  
43  
44  
45  
46  
47  
48  
49  
50  
51  
52  
53  
54  
55  
56  
57  
58  
59  
60  
61  
62  
63  
64  
65

1  
2 in phosphorylation barcodes with changes in physiology (Busillo et al., 2010; Butcher et al., 2011; Nobles et al.,  
3  
4 2011). There remains limited evidence that specific phosphopeptide patterns promote changes in receptor  
5 signaling with downstream physiological effects, and understanding how ligands generate such signaling profiles  
6  
7 is critical to understanding cellular signal transduction.  
8  
9

10  
11 The physiological relevance of endogenous biased signaling can be difficult to assess as the majority of  
12  
13 GPCR biased agonists are synthetic. However, many endogenous biased agonists have been identified in the  
14 chemokine system (Corbisier et al., 2015; Rajagopal et al., 2013), which consists of approximately 20 receptors  
15  
16 and 50 chemokine ligands (Eiger et al., 2021; Griffith et al., 2014; Kufareva et al., 2015). Unlike other GPCR  
17  
18 subfamilies, chemokine receptors are promiscuous and often bind multiple chemokines with high affinity (Allen  
19  
20 et al., 2007; Zlotnik and Yoshie, 2012). For example, the chemokine receptor CXCR3, primarily expressed on  
21  
22 activated T cells, binds three endogenous ligands, CXCL9, CXCL10, and CXCL11, and plays an important role  
23  
24 in inflammatory diseases and cancer (Chow et al., 2019; Kuo et al., 2018; Smith et al., 2018c). Like most other  
25  
26 chemokine receptors, CXCR3 signals through both Gαi family G proteins and β-arrestins (Colvin et al., 2006;  
27  
28 Colvin et al., 2004; Smith et al., 2017). CXCL11 is β-arrestin-biased compared to CXCL9 and CXCL10, with each  
29  
30 chemokine displaying distinct profiles of G protein signaling, β-arrestin recruitment and receptor internalization  
31  
32 (Rajagopal et al., 2013; Zheng et al., 2022). Synthetic CXCR3 biased agonists have shown distinct physiological  
33  
34 effects in a mouse model of allergic contact dermatitis, with a β-arrestin-biased agonist promoting inflammation  
35  
36 through increased T cell recruitment (Smith et al., 2018a). CXCR3 is well-suited for studying the mechanisms  
37  
38 underlying biased agonism and its physiological impact.  
39  
40

41  
42 It is unclear how receptors with multiple endogenous ligands encode divergent cellular signaling and  
43 function. Here we demonstrate that endogenous chemokines of CXCR3 encode unique phosphorylation barcode  
44  
45 ensembles (different phosphopeptides at different stoichiometries). These differential phosphorylation  
46  
47 ensembles lead to different patterns of transducer and kinase activation with subsequent distinctive chemotactic  
48  
49 patterns. Through mutagenic studies, we determined that CXCR3 biased signaling is encoded through the  
50  
51 receptor core and differential phosphorylation of the receptor C-terminal tail.  
52  
53  
54  
55  
56  
57

58  
59  
60 **RESULTS**  
61  
62  
63  
64  
65

1  
2 **CXCR3 chemokines promote different receptor phosphorylation barcode ensembles**  
3

4 CXCR3 chemokines (CXCL9, CXCL10, CXCL11) promote different levels of receptor phosphorylation  
5 (Colvin et al., 2004; Smith et al., 2017). However, it is not known whether this is due to differences of  
6 phosphorylation levels at the same sites or at different sites on the C-terminus, or both. To determine if the  
7 endogenous CXCR3 chemokines produce different phosphorylation barcode ensembles (different site patterns  
8 and levels of those patterns), we utilized state-of-the-art mass spectrometry with combinatorial phosphopeptide  
9 reference libraries with heavy isotope labeled reference standards corresponding to potential CXCR3 serine and  
10 threonine phosphorylation patterns as previously described (Tsai et al., 2019). This approach allowed us to not  
11 only identify but also quantify the relative abundance of specific phosphopeptides after chemokine stimulation.  
12 Wild-type human CXCR3-overexpressing HEK293 cells were stimulated with CXCL9, CXCL10, CXCL11 or  
13 vehicle control, followed by tryptic digestion and tandem mass tag (TMT) labelling, allowing samples to be pooled  
14 and greatly improving measurement precision as well as eliminating variability from batch effects (**Figure 1A**  
15 and **1B**). After ion metal affinity chromatography (IMAC) enrichment, TMT-labeled peptides were analyzed using  
16 liquid chromatography and tandem mass spectrometry (LC-MS/MS) for phosphopeptide identification (**Figure**  
17 **1B**). Phosphosites of interest were further validated by targeted proteomics with the addition of a synthetic library  
18 of 128 heavy isotope-labeled C-terminal phosphopeptides prior to IMAC enrichment. This enabled us to  
19 confidently differentiate and quantify adjacent phosphosites, providing high-resolution insights into the ensemble  
20 of receptor phosphopeptides following chemokine stimulation.

21 We identified several specific phosphopeptides following chemokine treatment (**Figure 1C**). We detected  
22 that every putative serine or threonine phosphorylation site on the RDSSWSETSEASYSGL tryptic peptide could  
23 be phosphorylated, although the levels of these phosphopeptides differed depending on chemokine treatment.  
24 For example, the abundance of the singly phosphorylated peptide DSSWSETSEASYpSGL (S366) significantly  
25 increased following treatment with CXCL9 but did not change with CXCL10 or CXCL11, providing direct evidence  
26 that the chemokines encode distinct GPCR phosphorylation ensembles (**Figure 1D**). We additionally detected a  
27 decrease in abundance of singly phosphorylated peptides at S355, S356, and T360 following treatment with all  
28 chemokines (**Figure S1A-S1C**), consistent with a loss of some singly phosphorylated peptides following ligand  
29 treatment, as the ensemble of barcodes shift towards those that were multiply phosphorylated.

1  
2  
3  
4 **Phosphorylation barcode ensembles direct G protein activation, β-arrestin recruitment, and receptor**  
5  
6 **internalization**  
7

8  
9 To study the effects of different phosphorylation barcode ensembles on cellular signaling, we screened  
10  
11 a variety of phosphorylation-deficient CXCR3 mutants (**Figure S1D-S1G**), either serine/threonine to alanine  
12  
13 mutants or truncation mutants, using G protein and β-arrestin assays. Based on this screen, we selected four  
14  
15 phosphorylation deficient receptors to interrogate in detail (**Figure 1E**). These receptors maintained cell surface  
16  
17 expression similar to wild-type CXCR3 (CXCR3-WT) (**Figure S1H**).  
18

19  
20 We first employed the TRUPATH bioluminescence resonance energy transfer (BRET) assay to assess  
21  
22 G protein activation (Olsen et al., 2020) (**Figure 2A**). Most C-terminal mutations did not impact CXCR3 G protein  
23  
24 activation, with similar profiles of CXCL11 and CXCL10 and reduced potency and  $E_{max}$  of CXCL9, as previously  
25  
26 described (Smith et al., 2017) (**Figure 2B-2D**). We did observe a significant left shift in the EC<sub>50</sub> of the truncation  
27  
28 mutant CXCR3-L344X at CXCL10 and CXCL11, consistent with increased G protein signaling (**Figure 2C** and  
29  
30 **2D**). When experiments were repeated in β-arrestin-1/2 CRISPR KO cells, CXCR3-WT potency was also left  
31  
32 shifted and indistinguishable from the truncation mutant, consistent with CXCR3-L344X increased G protein  
33  
34 signaling being due to a loss of β-arrestin-mediated desensitization (**Figure 2G**). Notably, we observed an  
35  
36 approximately 50% decrease in G protein activation at the phosphorylation deficient mutant CXCR3-  
37  
38 S355A/S356A (**Figure 2F**), which was not due to increased β-arrestin desensitization (**Figure S2A-S2D**), and  
39  
40 was partially rescued using a phosphomimetic mutant, CXCR3-S355D/S356D (**Figure S2E-S2G**), consistent  
41  
42 with receptor phosphorylation at specific sites impacting G protein activation.  
43  
44

45  
46 We next examined β-arrestin recruitment (**Figure 2H**). Consistent with prior work, CXCL11 was  
47  
48 significantly more effective in recruiting β-arrestin to CXCR3-WT compared to CXCL9 and CXCL10 (**Figure 2I-**  
49  
50 **K**) (Colvin et al., 2004; Smith et al., 2017; Zheng et al., 2022). All phosphodeficient mutant receptors treated with  
51  
52 CXCL11 demonstrated significantly less recruitment of β-arrestin when compared to CXCR3-WT (**Figure 2K**).  
53  
54 In contrast, few mutant receptors treated with CXCL9 and CXCL10 demonstrated changes in β-arrestin  
55  
56 recruitment relative to wild type (**Figure 2I-2J**). Differential β-arrestin recruitment was observed between  
57  
58 chemokines at CXCR3-WT, CXCR3-S355A/S356A, and CXCR3-T360A/S361A (**Figure S2H-S2L**). In contrast,  
59  
60  
61  
62  
63  
64  
65

1 we observed no difference between chemokines in their ability to recruit  $\beta$ -arrestin to receptor mutants lacking  
2  
3 the most putative C-terminal phosphorylation sites (CXCR3-4xA and CXCR3-L344X). This is consistent with  
4  
5 CXCR3 C-terminal phosphorylation sites being critical for differences in  $\beta$ -arrestin recruitment between  
6  
7 chemokines.  
8

9  
10 We next explored the impact of phosphodeficient CXCR3 receptors on  $\beta$ -arrestin function.  $\beta$ -arrestins  
11  
12 are known to regulate GPCR endocytosis by interacting with the clathrin adaptor protein AP-2 (Ferguson et al.,  
13  
14 1996; Kim and Benovic, 2002; Laporte et al., 1999). Therefore, we hypothesized that CXCR3 C-terminal  
15  
16 mutations would impair receptor internalization. We used confocal microscopy to monitor CXCR3 and  $\beta$ -arrestin  
17  
18 localization following chemokine treatment. CXCL11 promoted the translocation of CXCR3-WT and  $\beta$ -arrestin-2  
19  
20 to endosomes (**Figure 2L** and **Figure S3A**). CXCL10 also promoted CXCR3-WT: $\beta$ -arrestin puncta, but not to  
21  
22 the magnitude of CXCL11 (**Figure S3A**). CXCL9 did not promote either CXCR3-WT: $\beta$ -arrestin puncta or receptor  
23  
24 internalization (**Figure S3A**). Consistent with our hypothesis, CXCL10 or CXCL11 treatment of phosphorylation-  
25  
26 deficient CXCR3 mutants impaired internalization (**Figure 2L and S3B-S3E**).  
27  
28

29 To further evaluate and quantify internalization, we utilized a BRET-based assay to measure receptor  
30  
31 trafficking to early endosomes (**Figure 2M**). CXCL9 treatment did not induce significant CXCR3-WT endosomal  
32  
33 trafficking (**Figure 2N**). While CXCL10 promoted receptor internalization, none of the phosphorylation-deficient  
34  
35 mutants internalized after CXCL10 treatment. In contrast, CXCL11 treatment led to a different endosomal  
36  
37 trafficking pattern at mutant receptors, with CXCR3-S355A/S356A, -T360A/S361A, and -4xA internalizing~50%  
38  
39 of the level of CXCR3-WT, while CXCR3-L344X did not internalize at all. We confirmed these findings with an  
40  
41 orthogonal BRET assay to assess CXCR3 trafficking away from the plasma membrane following chemokine  
42  
43 treatment (**Figure S3F-S3G**). These results are consistent with ligand- and receptor-specific effects on  
44  
45 internalization: while removing selected phosphosites is sufficient to seemingly eliminate CXCL10-mediated  
46  
47 internalization, removal is not sufficient to completely inhibit CXCL11-mediated internalization. In contrast, the  
48  
49 receptor C-terminus is required for receptor internalization with CXCL10 and CXCL11, despite partial  $\beta$ -arrestin  
50  
51 recruitment to the CXCR3-L344X mutant.  
52  
53  
54

55  
56  
57  
58  
59  
60 **GRK2 and GRK3 are differentially recruited to CXCR3 following ligand stimulation**  
61  
62  
63  
64  
65

1            We next investigated the kinases critical to differential CXCR3 phosphorylation barcode ensembles.  
2  
3

4            While multiple kinases have been identified that phosphorylate GPCRs, the GRKs are established to be the  
5 primary drivers of GPCR phosphorylation (Gurevich and Gurevich, 2019; Komolov and Benovic, 2018; Tobin,  
6  
7 2008). There are seven identified GRK isoforms, of which GRK2, 3, 5, and 6 are ubiquitously expressed in  
8 mammalian tissues (Ribas et al., 2007). Because CXCR3 is primarily expressed on leukocytes, we investigated  
9 GRKs 2, 3, 5 and 6 recruitment to CXCR3 following chemokine treatment using a previously validated nanoBiT  
10 complementation assay (Inoue et al., 2019). We observed that GRK2 and GRK3 were recruited to all CXCR3  
11 mutant receptors following chemokine treatment with similar kinetic profiles (**Figure 3A-3F**). In contrast, we did  
12 not observe appreciable recruitment of GRK5 or GRK6 to CXCR3-WT or mutant receptors, and confirmed it was  
13 not due to competition between GRK isoforms by demonstrating a lack of GRK5 and 6 recruitment in GRK2/3/5/6  
14 knock out (KO) cells (Pandey et al., 2021a) (**Figure S4**).  
15  
16

17            At CXCR3-WT, CXCL9, CXCL10, and CXCL11 demonstrated similar maximal recruitment of GRK2 and

18            GRK3 (**Figure S5A** and **Figure S5L**). The effects of CXCR3 C-terminal mutations were variable (**Figure S5B-E**  
19 and **S5M-P**), with effects that were both chemokine- and receptor-dependent. At CXCR3-L344X, GRK2 and  
20 GRK3 recruitment was largely preserved with CXCL9 stimulation, but significantly reduced with CXCL10 or  
21 CXCL11 treatment (**Figure 3A-3C**). Surprisingly, two phosphodeficient mutants enhanced GRK recruitment to  
22 the receptor. To investigate this, we generated the phosphomimetic mutants CXCR3-T360D/S361D and CXCR3-  
23 4xD and found that they displayed decreased recruitment of GRK2 and GRK3, similar to that of CXCR3-WT  
24 (**Figure S5F-S5K** and **S5Q-S5V**). These results suggest that basal phosphorylation of specific residues in the  
25 C-terminus inhibit GRK recruitment. Together, these experiments demonstrate that GRK recruitment depends  
26 on both the specific C-terminal residue as well as the ligand used to activate the receptor.  
27  
28

### 29            **β-arrestin conformation is dependent on ligand identity and receptor phosphorylation status** 30

31            We next investigated how chemokines modulate β-arrestin conformation. Previous work has shown that

32 β-arrestins adopt multiple conformational states when engaged with the receptor core and C-terminus, and that  
33 these different states are important for β-arrestin-dependent signaling (Dwivedi-Agnihotri et al., 2020; Gurevich  
34 and Gurevich, 2004; He et al., 2021; Latorraca et al., 2020; Shukla et al., 2008; Xiao et al., 2004). We used a  
35  
36

1 previously validated intramolecular fluorescent arsenical hairpin (FIAsH) BRET assay to assess β-arrestin  
2 conformation (**Figure 3G and 3H**) (Lee et al., 2016) at all five mutant CXCR3 receptors treated with CXCL9,  
3 CXCL10, or CXCL11. Data are presented as radar plots, enabling simultaneous visualization of all FIAsH  
4 biosensors at each receptor:ligand combination (**Figure 3I-3P**, conformation heat maps and bar charts  
5 corresponding to FIAsH signals are shown in **Figure S6A-S6F, S6G**). At CXCR3-WT, we found that CXCL9 did  
6 not induce a significant conformational change compared to vehicle, while both CXCL10 and CXCL11 promoted  
7 significant changes in the β-arrestin C-domain (FIAsH 4,5) and C-terminus (FIAsH 6) (**Figure S6G**). Minimal  
8 conformational changes were noted in the N-domain of β-arrestin (FIAsH 1,2).  
9

10  
11 Analyzing conformational signatures by chemokine, phosphorylation-deficient mutants had no significant  
12 effect on β-arrestin conformational signatures following treatment with CXCL9 (**Figure 3I**) but had significant  
13 effects on the conformations when stimulated with CXCL10 and CXCL11 (**Figure 3J and 3K**). Analyzing  
14 conformational signatures by mutant, CXCR3-S355A/S356A abolished all chemokine-specific β-arrestin  
15 conformational signatures (**Figure 3M**). In contrast, CXCR3-T360A/S361A (**Figure 3N**) promoted a β-arrestin-2  
16 conformational signature nearly identical to CXCR3-WT (**Figure 3L**). CXCR3-4xA had decreased conformational  
17 changes in the β-arrestin C-domain (FIAsH 4 and 5) compared to CXCR3-WT, but with preserved conformational  
18 changes at the C-terminus (FIAsH 6) (**Figure 3O**). At CXCR3-L344X, nearly all conformational differences  
19 between chemokines were lost, with only small differences observed in the β-arrestin C-terminus between  
20 chemokines (FIAsH 6) (**Figure 3P**). These data suggest that, even in the absence of a C-terminus, the  
21 chemokines are still able to promote distinct β-arrestin-2 conformational signatures through the receptor core  
22 (**Figure S6G**). Phosphorylation sites in the C-terminus play a central role in determining β-arrestin 2  
23 conformation, with sites such as S355 and S356 being critical for biased G protein activation, β-arrestin  
24 recruitment, and β-arrestin conformation.  
25

26  
27 These data further show that the conformational status of the N-domain (FIAsH 1,2) depends on the  
28 identity of the chemokine and receptor, but that these effects are largely independent of each other (**Figure S6A**  
29 and **S6B**). However, the totality of conformational data demonstrates that the conformational signature of the C-  
30 domain (FIAsH 4 and 5) and C-terminus (FIAsH 6) of β-arrestin is distinctively dependent on the combination,  
31 rather than additive effects of chemokine identity and CXCR3 phosphorylation status (**Figure S6D-S6F**).  
32  
33  
34  
35  
36  
37  
38  
39  
40  
41  
42  
43  
44  
45  
46  
47  
48  
49  
50  
51  
52  
53  
54  
55  
56  
57  
58  
59  
60  
61  
62  
63  
64  
65

1  
2  
3

4 **Molecular Dynamic Studies of β-arrestin**  
5

6  
7 To better characterize the conformational changes of β-arrestin observed using FlAsH probes, we  
8  
9 performed structural modeling and computer simulation. The exact location of probes 1-3 in the N-domain and  
10  
11 probes 4-5 in the structured beta-sheets of the C-domain are highlighted in our structural model of β-arrestin-2  
12  
13 fused to RLuc (**Figure S7**). As probe 6 is located within the distal C-tail, a highly flexible region which currently  
14  
15 has not been crystallized, it is absent from our structural model and further analysis.  
16

17  
18 According to the BRET data, the signal from probes 1-3 (located in the N-domain) was similar in the  
19  
20 presence of different chemokines (**Figure 3I-3K**) or C-tail mutations (**Figure 3L-3P**). This suggests that the  
21  
22 relative position of the N-domain and RLuc to each other do not significantly change in those conditions. In  
23  
24 contrast, we observed that probes 4 and 5 located in the C-domain are sensitive to different chemokines and C-  
25  
26 tail mutations. This indicates that structural changes induced in β-arrestin 2 by the receptor and the type of  
27  
28 chemokine ligand result in a significant positional change of the C-domain with respect to the RLuc-fused N-  
29  
30 domain. Such observed conformational changes are likely the result of receptor-induced activation of β-arrestin  
31  
32 2. Interestingly, previous studies have highlighted that this activation of arrestin is linked to a twist of the C-  
33  
34 terminal domain in respect to the N-domain (Chen et al., 2017; Dwivedi-Agnihotri et al., 2020; Latorraca et al.,  
35  
36 2018; Shukla et al., 2013). This transition can be quantified using the interdomain rotation angle, with higher  
37  
38 values of this angle being linked to more active-like conformations of β-arrestin and vice versa (**Figure S7**).  
39  
40

41  
42 To investigate whether the interdomain twist correlates with the distance between probes 4 or 5 and the  
43  
44 RLuc anchor point (Arg8), we monitored both descriptors in β-arrestin simulations starting from an active-like  
45  
46 conformation (**Figure 4A**). As we did not include either the receptor or a C-tail in the system, such a setup allows  
47  
48 β-arrestin to spontaneously inactivate (Latorraca et al., 2018) and to sample interdomain rotation angles from 20  
49  
50 (active-like state) to 0 degrees (inactive-like state). Importantly, our simulations confirm that there is indeed a  
51  
52 correlation between the RLuc-probe 4/5 distances and the interdomain rotation angles ( $R=0.54$  for probe 4 and  
53  
54  $R=0.65$  for probe 5). This suggests that these probes are sensitive to the activation state of β-arrestin 2. In  
55  
56 contrast, the distances for probes 1-3 in the N-domain did not show any correlation with the value of the  
57  
58 interdomain twist.  
59  
60

61  
62  
63  
64  
65

1 To further verify this finding, we simulated β-arrestin 2 in complex with each of the studied CXCR3 C-tail  
2 variants (**Figure 4B**) and monitored their interdomain rotation angles (**Figure 4C**). We found that the WT samples  
3 primarily conformations with a rotation angle of 14°. A similar ensemble of conformations was also observed for  
4 the T360A/S361A mutant (peak 11°). Interestingly, the 4xA mutant showed a reduction in rotation angle whereas  
5 the strongest shift towards low rotation angles was found for the S355A/S356A and L344X mutants (peaks at 6°  
6 and 4°). The order of adopted rotation angles is consistent with the magnitude of BRET signal for FlAsH probes  
7 4 and 5, demonstrating that these probes are useful tools to approximate β-arrestin activation.

8  
9 β-arrestin structural dynamics provides a potential explanation for the induced conformational differences  
10 by specific C-tail mutants. We found that in the WT receptor, two negatively charged residues present in the C-  
11 tail (phosphorylated S358 and E359) form a bifurcated interaction with the positively charged residue K295  
12 located in the lariat loop of β-arrestin 2 (**Figure 4B**, blue region). We observed that in systems which explore  
13 more active-like conformations (e.g., WT and T360A/S361A), there were, on average, more interactions between  
14 the lariat loop and the C-tail in comparison to systems that explored more inactive-like states (e.g., 4xA,  
15 S355A/S356A, L344X) (**Figure 4C**). Importantly, these findings are consistent with previous studies that have  
16 demonstrated that polar interactions of the C-tail with the lariat loop are functionally important (Baidya et al.,  
17 2020) and promote active-like conformations of β-arrestin (Dwivedi-Agnihotri et al., 2020).

18  
19  
20  
**21 Global LC-MS proteomic and phosphoproteomic analyses reveal substantial variation in intracellular**  
22 **23 signaling between CXCL9, CXCL10, and CXCL11**

24 To further understand the breadth of intracellular signaling promoted by CXCR3 chemokines, we  
25 interrogated the global proteome of HEK293 cells treated with CXCL9, CXCL10, or CXCL11 (**Figure S8A**). We  
26 successfully identified over 150,000 total peptides corresponding to approximately 11,000 proteins. Of these  
27 peptides, approximately 30,000 were also identified as phosphopeptides corresponding to approximately 5,500  
28 unique phosphoproteins (**Figure S8B** and **S8C**). The majority of identified phosphosites were phosphoserines  
29 and phosphothreonines, with a high degree of reproducibility across replicates (**Figure S8D** and **S8E**). We  
30 identified approximately 1,500 phosphopeptides that underwent significant changes in abundance following  
31 chemokine treatment (**Figure 5A**). We then performed a clustering analysis of those phosphopeptides to uncover  
32 coregulated signaling pathways (Rigbolt et al., 2011) (**Figure S8F**). Certain signaling pathway clusters were  
33

1 similar between the three chemokines, while other clusters demonstrated significant differences between  
2 treatments (**Figure 5B**). Gene ontology term enrichment was performed on the significantly divergent  
3 phosphopeptides to assess the biological processes, molecular functions, and cellular compartments regulated  
4 by CXCR3 (**Figure 5C-5E**). These analyses reveal differential regulation of cellular transcription, post-  
5 translational modifications, cytoskeletal rearrangements, and cellular migration (among others) between  
6 chemokines. Additionally, the nucleus, cytoplasm, cytoskeleton, and cell-cell junctions were the most identified  
7 cellular compartments found in our gene ontology analysis. These data also show that CXCR3 chemokines do  
8 not signal in a purely redundant manner and display a striking degree of heterogeneity across signaling pathways  
9 associated with multiple cellular functions and compartments.  
10  
11  
12  
13  
14  
15  
16  
17  
18  
19  
20  
21  
22  
23  
24  
25  
26  
27  
28  
29  
30  
31  
32  
33  
34  
35  
36  
37  
38  
39  
40  
41  
42  
43  
44  
45  
46  
47  
48  
49  
50  
51  
52  
53  
54  
55  
56  
57  
58  
59  
60  
61  
62  
63  
64  
65

#### 302 **Biased CXCR3 phosphorylation serves as a mechanism underlying differential regulation of the kinome**

303 We next investigated the kinases responsible for generating chemokine-specific phosphorylation-  
304 dependent signaling networks. Kinase enrichment analyses (Lachmann and Ma'ayan, 2009) revealed that our  
305 dataset was largely enriched for phosphopeptides substrates targeted by cyclin dependent kinases (CDKs) and  
306 mitogen-activated protein kinases (MAPKs) (**Figure 5F**). We next used Modification Motifs, a motif-based  
307 sequence analysis tool (Bailey et al., 2006; Cheng et al., 2019), to identify enriched amino acid motifs flanking  
308 the phosphoserines and phosphothreonines that were differentially regulated in our dataset. Four major  
309 consensus sequences were identified: pS/pT-P which is a conserved target sequence of CDKs and MAPKs, R-  
310 X-X-pS/pT which is targeted by protein kinase B (Akt), pS/pT-L, and pS/pT-X-X-E which is targeted by casein  
311 kinase 2 (**Figure 5G**). These findings are consistent with previous studies demonstrating that CXCR3 activates  
312 the MAPK extracellular signal-related kinase (ERK) and Akt, among others (Bonacchi et al., 2001; Smith et al.,  
313 2018a), but also reveal unexplored CXCR3 signaling networks.  
314  
315 Next, we manually identified differentially phosphorylated kinases in our global phosphoproteomic data  
316 that are known to be regulated by GPCRs, or that were identified in bioinformatics analyses (**Figure 6A-6F**). The  
317 MAPKs ERK1, RAF1 and JNK, as well as SRC kinase family were phosphorylated in a chemokine-specific  
318 pattern, whereas BRAF and CSNK2 demonstrated similar phosphorylation patterns across CXCL9, CXCL10,  
319 and CXCL11. To understand if this biased regulation of the kinome is regulated by CXCR3 receptor

1 phosphorylation, we studied ERK1/2 phosphorylation following chemokine treatment of cells expressing either  
2 CXCR3-WT or a phosphodeficient CXCR3 mutant (**Figure 6G-6J**). At CXCR3-WT, we saw a significant increase  
3 in phosphorylated ERK1/2 (pERK), consistent with our mass spectrometry results (**Figure S9A**). At 5 minutes,  
4 we observed a maximum increase in pERK levels over CXCR3-WT at CXCR3-4xA and CXCR3-L344X when  
5 stimulated with CXCL10 and CXCL11, but not CXCL9. At 30 and 60 minutes, pERK levels declined, consistent  
6 with prior observations at other GPCRs (Luttrell et al., 2018). This differential phosphorylation of ERK1/2 by the  
7 three chemokines was observed at all mutant CXCR3 receptors, including CXCR3-L344X (**Figure S9**).  
8  
9  
10  
11  
12  
13  
14  
15  
16  
17  
18  
19  
20  
21

### 22 **T cell chemotaxis is regulated by biased CXCR3 phosphorylation barcode ensembles** 23

24 We last investigated if the biased chemokine signaling pathways observed in HEK293 cells impact  
25 physiologically relevant cellular functions. Given that CXCR3 plays a central role in T cell function, we  
26 interrogated the effect of CXCR3 phosphorylation barcodes on T cell chemotaxis. We first used CRISPR/Cas9  
27 to knock out the endogenous CXCR3 in Jurkat cells (an immortalized human T lymphocyte cell line), generating  
28  
29 CXCR3 knockout (CXCR3-KO) Jurkats. We rescued CXCR3 receptors of interest (WT and mutants) with  
30  
31 lentiviral constructs to generate stably expressing CXCR3+ Jurkat cell lines (**Figure 7A**). We confirmed similar  
32  
33 receptor expression levels between WT and mutant CXCR3+ Jurkat lines (**Figure 7B**).  
34  
35  
36

37 We then performed chemotaxis assays with these cell lines. Due to the promiscuous nature of the  
38 chemokine system, we first confirmed that CXCR3-KO Jurkats exhibit no measurable chemotaxis compared to  
39 vehicle treatment (**Figure 7C**), demonstrating that the observed chemotactic response is mediated by CXCR3  
40 and not by other chemokine receptors. CXCR3+ Jurkat cells migrated with different chemotactic indices to  
41 CXCL9, CXCL10, or CXCL11, consistent with a biased response across chemokines. Statistically, there were  
42 effects induced both by ligand and by receptor (**Figure S10A-S10F**). We observed a slight but significant  
43 decrease in chemotactic function at CXCR3-S355A/S356A and CXCR3-T360A/S361A with CXCL11, but not  
44 with CXCL9 nor CXCL10. Conversely, we observed a significant increase in chemotaxis with CXCL11 at CXCR3-  
45 4xA and CXCR3-L344X, although with different patterns. While chemotaxis at CXCR3-4xA displayed the same  
46 pattern by chemokine as CXCR3-WT (CXCL11 > CXCL9 > CXCL10), chemotaxis at CXCR3-L344X displayed  
47  
48  
49  
50  
51  
52  
53  
54  
55  
56  
57  
58  
59  
60  
61  
62  
63  
64  
65

1  
345 2 only minor differences between all chemokines, although all displayed significantly more chemotaxis than at  
3  
346 4 CXCR3-WT.  
5  
6  
7  
8

348 9 **Associating T cell chemotaxis with transducer efficacy**

10  
349 11 The biased pattern of chemotaxis at all receptors except L344X was different than that observed at  
12  
350 13 proximal GPCR signaling assays, i.e., G protein activation and β-arrestin recruitment. To ascertain if G protein  
14  
351 15 or β-arrestin signaling was directly related to chemotactic function, we performed univariate linear regressions  
16  
352 17 on these data and found no significant linear relationship between G protein or β-arrestin signaling efficacy and  
18  
353 19 chemotactic function (**Figure S10G-S10H**). We then performed a principal component analysis of G protein  
20  
354 21 signaling and β-arrestin signaling versus chemotactic function and similarly found no obvious clustering of data  
22  
355 23 by ligand or receptor (**Figure 7D**). A univariate linear regression of MAPK activation versus chemotactic function  
24  
356 25 did demonstrate a significant positive linear relationship (**Figure S10I**). We then performed a second principal  
26  
357 27 component analysis of all major assays conducted in this study and were able to demonstrate clustering of the  
28  
358 29 chemokines at CXCR3-L344X (**Figure 7E**). These analyses demonstrated that G protein and β-arrestin signaling  
30  
359 31 alone or together do not comprehensively describe the observed variance in our functional assays. Further  
32  
360 33 addition of other signaling data (GRK recruitment, FlASH conformational assays) moderately enhanced our ability  
34  
361 35 to describe the variance in cellular chemotaxis, however, only at CXCR3-L344X. For receptors with a C-terminal  
362 36 tail, their chemotactic profiles did not cluster after PCA analysis, consistent with the C-terminus contributing to a  
37  
363 38 biased response even when differences in transducer coupling are accounted for. Together, these data support  
39  
364 40 a working model in which biased chemokines promote bias through the receptor core and through different  
41  
365 42 CXCR3 phosphorylation barcode ensembles that regulate both proximal and distal aspects of GPCR signaling  
43  
366 44 that impact T cell chemotaxis in a complex fashion (**Figure 7F**).  
45  
367 46  
368 47  
369 48  
370 49  
371 50  
372 51  
373 52  
374 53  
375 54

**DISCUSSION**

55  
369 56 Here we report how different chemokines for the same receptor direct distinct signaling pathways. We  
57  
370 58 conclusively demonstrate that the endogenous chemokines of CXCR3 have biased patterns of signaling and are  
59  
371 60 nonredundant in their activation of different intracellular kinase cascades and chemotactic profiles. Signal  
61  
62  
63  
64  
65

1 initiation through G proteins and  $\beta$ -arrestins, well-conserved effectors across the GPCR superfamily, is directed  
2 by CXCR3 C-terminus phosphorylation, whereby the different chemokines encode distinct phosphorylation  
3 ensembles. Disrupting discrete CXCR3 phosphorylation patterns interfered with signaling downstream of certain  
4 CXCR3 chemokines, but not others, depending on the phosphorylation site. Disrupting certain phosphosites also  
5 altered T cell function as assessed by chemotaxis, and this complex physiological output could not be entirely  
6 defined by the activity of proximal G protein or  $\beta$ -arrestin transducers alone.  
7

8         Using multiple high-resolution mass spectrometry approaches, we found that different chemokines  
9 promoted different CXCR3 phosphorylation barcode ensembles. Limitations of mass spectrometry-based  
10 approaches in studying the phosphorylation of transmembrane receptors include their relative low abundance,  
11 difficulty in isolation, and sample handling demands. To overcome these challenges, we incorporated and  
12 validated a combinatorial phosphopeptide library with heavy isotope-labeled reference standards (Tsai et al.,  
13 2019), allowing us to simultaneously analyze wild-type, untagged CXCR3 under different chemokine treatment  
14 conditions. We found that perturbations in specific phosphorylation patterns impact proximal and distal aspects  
15 of GPCR signaling, as well as chemotaxis. At GPCRs more broadly, there is limited work investigating the  
16 phosphorylation patterns generated by endogenous ligands (Busillo et al., 2010), as most studies have relied on  
17 synthetic ligands (Butcher et al., 2011; Miess et al., 2018; Nobles et al., 2011). In addition, there is a desire to  
18 develop biased therapeutics which preferentially activate signaling pathways to increase therapeutic efficacy  
19 while simultaneously decreasing side effects, and our findings could provide an initial methodology to screen  
20 ligands for a desired physiological output. Our results demonstrate that the GPCR C-terminus is critically  
21 important in the regulation of proximal signaling effectors, and that the final cellular phenotype is dependent on  
22 the integration of multiple signaling pathways downstream of these interactions.  
23

24         We found that both the receptor core and distinct phosphorylation patterns in the tail contribute to the  
25 allosteric regulation of  $\beta$ -arrestin conformation.  $\beta$ -arrestins can engage GPCRs through independent interactions  
26 with the receptor core and C-terminus (Cahill et al., 2017; Eichel et al., 2018; Kahsai et al., 2018; Latorraca et  
27 al., 2018). We found that all chemokine agonists similarly recruited  $\beta$ -arrestin to the receptor core in the absence  
28 of a C-terminus but maintained the ability to promote different  $\beta$ -arrestin conformations. Additionally, although  $\beta$ -  
29 arrestin-2 could still recruit to CXCR3-L344X, the receptor did not internalize, highlighting the importance of the  
30 C-terminus in this process. Interestingly, the C-terminal tail of CXCR3-L344X was able to recruit  $\beta$ -arrestin-1, but  
31 not  $\beta$ -arrestin-2, suggesting differential recruitment of  $\beta$ -arrestin isoforms based on the presence of the C-terminus.  
32         In conclusion, we have demonstrated that the C-terminus of CXCR3 is critical for its proximal signaling  
33 effectors, and that the C-terminus is required for the recruitment of  $\beta$ -arrestin. Our findings highlight the  
34 importance of the C-terminus in the regulation of GPCR signaling, and provide a methodology to study the  
35 C-terminus of GPCRs. This work will facilitate the development of biased therapeutics which target the C-terminus  
36 of GPCRs to achieve desired physiological outputs. Future work will focus on understanding the molecular  
37 mechanisms through which the C-terminus regulates GPCR signaling, and how this knowledge can be  
38 applied to the development of new therapeutics. Overall, our findings demonstrate the critical role of the C-terminus  
39 in GPCR signaling, and provide a foundation for future research in this field.  
40

1  
399 2 β-arrestin-2 interaction with the receptor C-terminus in promoting receptor internalization as previously described  
3  
400 4 (Cahill et al., 2017). Our findings agree with recent studies demonstrating that not all phosphorylation sites on a  
5  
401 6 GPCR C-terminus impact β-arrestin recruitment and function (Dwivedi-Agnihotri et al., 2020; Latorraca et al.,  
7  
402 8 2020). PCA analysis of signaling and chemotaxis data support a model in which chemokines promote bias  
9  
403 10 through both the receptor core and CXCR3 phosphorylation barcode ensembles that regulate both proximal and  
11  
404 12 distal aspects of GPCR signaling.  
13  
405 14

15  
406 16 While previous studies demonstrated that certain C-terminal phosphorylation sites are involved in β-  
17  
407 18 arrestin conformation, many of these studies have been limited to *in vitro* and *in silico* methods (Sente et al.,  
19  
408 20 2018; Zhou et al., 2017). Here, we demonstrate in a cellular context that the β-arrestin conformation formed at a  
21  
409 22 GPCR is dependent on the specific combination of both the ligand and the receptor phosphorylation pattern.  
23  
410 24 Importantly, the conformational diversity seen in the C-domain and C-terminus of β-arrestin cannot be explained  
25  
411 26 simply through the additive effects of ligand and receptor identity. Rather, the unique interaction between the  
27  
412 28 ligand and receptor phosphorylation pattern ultimately promotes β-arrestin to adopt a specific ensemble of  
29  
413 30 conformations, highlighting the complex structural diversity a single GPCR can impose upon proximal effector  
31  
414 32 proteins like β-arrestin. Modeling and molecular dynamics simulations suggest that β-arrestin conformations vary  
33  
415 34 35 in the degree of interdomain rotation between the N- and C-domains. This motion has been previously described  
36  
416 37 to be a crucial step in β-arrestin activation (Latorraca et al., 2018). Our results show that certain chemokines and  
38  
417 39 C-tail mutants shift the conformational equilibrium of β-arrestin towards active-like conformations. Furthermore,  
40  
418 41 a more detailed analysis suggests that a specific pattern of interaction of the receptor C-tail with the lariat loop  
42  
43 44 region of β-arrestin contributes towards this transition.  
45  
46

419 47 This work also provides a comprehensive assessment of the roles biased agonists and receptor  
48  
420 49 phosphorylation serve in directing downstream signaling. Not only did we observed that chemokines induce  
50  
421 51 distinct phosphoproteomic signaling profiles through a single receptor, but we also demonstrate how specific  
52  
422 53 changes in CXCR3 phosphorylation barcodes impact the biased regulation of the phosphoproteome and MAPK  
54  
423 55 signaling. We identified a relationship between MAPK activation and chemotactic function, even though these  
56  
424 57 assays were performed in different cell types, consistent with previous studies (Shahabuddin et al., 2006; Sun  
58  
425 59 et al., 2002). Our data suggests that a systems-level approach integrating upstream and downstream signaling  
60  
61  
62  
63  
64  
65

1  
2 effectors will be critical to the development of novel therapeutics with a desired phenotype, rather than an  
3  
4 approach that relies solely on specific proximal transducers. Because protein-protein interfaces are frequent  
5  
6 pharmacologic targets and commonly regulated via phosphorylation, this investigative framework extends to  
7  
8 many other domains of pharmacology and cellular signaling (Stevens et al., 2018; Watanabe and Osada, 2012).  
9  
10  
11 Therefore, this study has important implications in understanding the pluridimensional efficacy of the chemokine  
12  
13 system, the GPCR superfamily, and all receptors more broadly.  
14

15  
16 Our findings prompt many avenues for future study. Importantly, there are technical limitations that must  
17  
18 be overcome to better determine the abundance of highly phosphorylated C-terminal peptides. Accurate  
19  
20 determination of the stoichiometry of physiologically relevant phosphorylation barcodes is critical to  
21  
22 understanding how these ensembles direct GPCR effector function under native conditions. Additionally, further  
23  
24 work is needed to elucidate the detailed mechanism underlying the generation of these barcode ensembles –  
25  
26 while we provide evidence demonstrating biased interactions of GRKs with CXCR3, it remains unclear how these  
27  
28 ligands target the GRKs and other kinases to specific locations within the C-terminus and receptor core. Notably,  
29  
30  
31 there is heterogenous expression of the GRKs and other kinases throughout the human body; therefore, it is  
32  
33 pertinent to understand how receptor phosphorylation may change depending on the effectors present to interact  
34  
35 with a GPCR (Sato et al., 2015). Also, while there is evidence of specific signaling cascades directly dependent  
36  
37 on G protein or β-arrestin activation, more complex cellular phenotypes are likely dependent on the combination  
38  
39 of these and other GPCR signaling partners. For example, there is burgeoning evidence of GPCR signaling  
40  
41 pathways that extend beyond that canonical G protein versus β-arrestin paradigm, specifically, those that  
42  
43 integrate these pathways together (Smith et al., 2021). Using systems-level approaches to characterize these  
44  
45 processes will be critical to understanding the coordination of signaling through different GPCR transducers.  
46  
47  
48

49 While it was a long-held belief that signaling in the chemokine system was redundant (Mantovani, 1999),  
50  
51 we conclusively demonstrate that signaling through the three endogenous chemokine agonists of CXCR3,  
52  
53 CXCL9, CXC10, and CXCL11 is not redundant. These three chemokines (1) encode distinct receptor  
54  
55 phosphorylation patterns, (2) promote strikingly divergent signaling profiles as assessed by ~30,000  
56  
57 phosphopeptides corresponding to ~5,500 unique phosphoproteins, and (3) promote distinct phosphosite-  
58  
59 dependent physiological effects as assessed by chemotaxis. We have previously shown in a mouse model of  
60  
61  
62  
63  
64  
65

1 contact hypersensitivity that a β-arrestin-biased CXCR3 agonist can increase inflammation whereas a G protein-  
2 biased CXCR3 agonist did not (Smith *et al.*, 2018a), further supporting the physiological relevance of biased  
3 signaling at CXCR3. Additionally, T cells derived from β-arrestin-2 KO mice demonstrate impaired chemotactic  
4 response in the presence of either a β-arrestin-biased or G protein biased CXCR3 agonist (Smith *et al.*, 2018a).  
5  
6 Taken as a whole, our findings suggest that cellular functions such chemotaxis are not merely encoded by the  
7 amount of β-arrestin recruited to the receptor, rather, it is influenced by specific β-arrestin conformations induced  
8 by a receptor (Ge *et al.*, 2003; Lin *et al.*, 2018; Yang *et al.*, 2015). The non-redundant nature of chemokine  
9 signaling at CXCR3 likely applies to the remainder of the chemokine system, although further work is necessary  
10 to confirm this hypothesis.  
11  
12  
13  
14  
15  
16  
17  
18  
19  
20  
21  
22  
23  
24  
25  
26  
27  
28  
29  
30  
31  
32  
33  
34  
35  
36  
37  
38  
39  
40  
41  
42  
43  
44  
45  
46  
47  
48  
49  
50  
51  
52  
53  
54  
55  
56  
57  
58  
59  
60  
61  
62  
63  
64  
65

1  
462 **ACKNOWLEDGEMENTS**  
2  
3

4 We thank R.J. Lefkowitz (Duke University, USA) for guidance, mentorship, and thoughtful feedback throughout  
5 this work; N. Nazo for laboratory assistance; R. Shammas for assistance with FIASH experiments. Funding: This  
6  
7 work was supported by T32GM007171 (D.S.E.), the Duke Medical Scientist Training Program (D.S.E.), AHA  
8  
9 20PRE35120592 (D.S.E.), 1R01GM122798 (S.R.), K08HL114643 (S.R.), Burroughs Wellcome Career Award  
10  
11 for Medical Scientists (S.R.), National Center of Science, Poland - 2017/27/N/NZ2/02571 (T.M.S.),  
12  
13 P41GM103493 (R.D.S.), 1R01GM139858 (T.S.). A.I. was funded by Japan Society for the Promotion of Science  
14  
15 (JSPS) KAKENHI grants 21H04791, 21H05113, JPJSBP120213501 and JPJSBP120218801; FOREST  
16  
17 Program JPMJFR215T and JST Moonshot Research and Development Program JPMJMS2023 from Japan  
18  
19 Science and Technology Agency (JST); The Uehara Memorial Foundation; and Daiichi Sankyo Foundation of  
20  
21 Life Science. Work was performed in the Environmental Molecular Sciences Laboratory, a U. S. Department of  
22  
23 Energy Office of Biological and Environmental Research national scientific user facility located at Pacific  
24  
25 Northwest National Laboratory in Richland, Washington. Pacific Northwest National Laboratory is operated by  
26  
27 Battelle for the U.S. Department of Energy under Contract No. DE-AC05-76RLO 1830.  
28  
29  
30  
31  
32  
33  
34  
35

477 **AUTHOR CONTRIBUTIONS**  
36  
37

478 Conceptualization, D.S.E., J.S.S., and S.R; Methodology, D.S.E., J.S.S., J.M.J, R.D.S., S.R., T.M.S., and J.D.S.;  
38  
39 Investigation, D.S.E., J.S.S., C.H., N.B., J.G., T.S., C.T., N.K., C.D.N., A.M.M., T.M.S, K.K., I.C., K.Z., A.W.,  
40  
41 P.A., N.M.K., O.H.; Resources, K.K.,A.I.; Writing - Original Draft, D.S.E., J.S.S., and S.R.; Writing – Reviewing  
42  
43 & Editing: D.S.E., J.S.S., and S.R, Visualization: D.S.E., J.S.S., and S.R; Supervision and Funding Acquisition,  
44  
45  
46 S.R.  
47  
48  
49  
50

484 **DECLARATION OF INTERESTS**  
51  
52

485 The authors declare no competing interests.  
53  
54

486 **INCLUSION AND DIVERSITY**  
55  
56  
57  
58  
59  
60  
61  
62  
63  
64  
65

1  
2 One or more of the authors of this paper self-identifies as an underrepresented ethnic minority in science. While  
3  
4 citing references scientifically relevant for this work, we also actively worked to promote gender balance in our  
5  
6 references list.  
7  
8  
9  
10  
11  
12  
13  
14  
15  
16  
17  
18  
19  
20  
21  
22  
23  
24  
25  
26  
27  
28  
29  
30  
31  
32  
33  
34  
35  
36  
37  
38  
39  
40  
41  
42  
43  
44  
45  
46  
47  
48  
49  
50  
51  
52  
53  
54  
55  
56  
57  
58  
59  
60  
61  
62  
63  
64  
65

1  
2 **MAIN FIGURE TITLES AND LEGENDS**  
3  
4  
5  
6

491 **Figure 1: Detection of CXCR3 C-terminal phosphopeptides using mass spectrometry**  
492  
493  
494

9 (A) Snake diagram of CXCR3 highlighting green putative C-terminal phosphorylation sites (S, T, and Y). (B)  
10  
495 Schematic of experimental design of receptor phosphoproteomics experiment. (C) Singly, doubly, and triply  
11  
496 phosphorylated CXCR3 C-terminal peptides identified through mass spectrometry. Identified phosphopeptides  
12  
497 are noted in red. (D) Abundance of singly phosphorylated DSSWSETSEASYpSGL peptide measured in HEK293  
13  
498 cells following stimulation with vehicle control or CXCL9, CXCL10, or CXCL11 at 100 nM for 5 minutes. Mean ±  
14  
499 SEM, n=2 technical replicates of 6 pooled biological replicates. (E) Diagram of designed CXCR3  
15  
500 phosphorylation-deficient receptor mutants of interest. \*P<.05, by one-way ANOVA, Tukey's post hoc analysis.  
16  
501 See S1 for additional mass spectrometry data and signaling and expression data of CXCR3 phosphorylation  
17  
502 deficient mutants.  
18  
503  
504 **Figure 2: G protein dissociation, β-arrestin-2 recruitment, and receptor internalization of CXCR3 and**  
505 **receptor mutants**  
506  
507

31 (A) Schematic of TRUPATH assay to detect G protein dissociation following receptor stimulation using BRET  
32  
508 (Olsen et al., 2020). (B, C, and D) G protein dissociation of receptors treated with listed chemokine in HEK293  
33  
509 cells. (E and F) G protein dissociation of CXCR3-WT and CXCR3-S355A/S356A in HEK293 cells. (G) G protein  
34  
510 dissociation of CXCR3-WT and CXCR3-L344X in wild-type HEK293 cells (WT HEK293) and β-arrestin-1/2 knock  
35  
511 out cells (βarr 1/2 KO). (H) Schematic of BRET assay to detect β-arrestin-2 recruitment to the receptor. (I, J, and  
36  
512 K) β-arrestin-2 recruitment of receptors treated with listed chemokine in HEK293 cells. (L) Representative  
37  
513 confocal microscopy images of HEK293 cells transfected with receptor-GFP and β-arrestin-2-RFP following  
38  
514 treatment with vehicle control or the listed chemokine for 45 minutes. Images are representative of three  
39  
515 biological replicates. (M) Schematic of BRET assay to detect receptor internalization to endosomes. (N) BRET  
40  
516 data of receptor internalization following stimulation with the listed chemokine. Data are the average of BRET  
41  
517 values from 20-30 minutes following ligand stimulation. For (A-G) TRUPATH assays, data shown are the mean  
42  
518 ± SEM of BRET values 5 to 10 minutes following ligand stimulation, n=3. \* denotes statistically significant  
43  
519  
44  
520  
45  
521  
46  
522  
47  
523  
48  
524  
49  
525  
50  
526  
51  
527  
528  
529  
530  
531  
532  
533  
534  
535  
536  
537  
538  
539  
540  
541  
542  
543  
544  
545  
546  
547  
548  
549  
550  
551  
552  
553  
554  
555  
556  
557  
558  
559  
560  
561  
562  
563  
564  
565

1 differences between  $E_{max}$  of specified receptor and CXCR3-WT. # denotes statistically significant differences  
2  
3  
4 between  $EC_{50}$  of specified receptor and CXCR3-WT. For  $\beta$ -arrestin-2 recruitment, data shown are the mean  $\pm$   
5 SEM, n=3. \*denotes statistically significant differences between  $E_{Max}$  of CXCR3-WT and all other receptors at  
6  
7 CXCL11, and of CXCR3-WT and CXCR3-4xA at CXCL9. # denotes statistically significant differences between  
8  
9  $EC_{50}$  of CXCR3-WT and CXCR3-S355A/S356A at CXCL10. For internalization BRET assays (**N**), data are the  
10  
11 mean  $\pm$  SEM, n=4. \*P<.05 by two-way ANOVA, Dunnett's post hoc testing between CXCR3-WT and all other  
12  
13 receptor mutants. See S2 and S3 for further data assessing G protein dissociation,  $\beta$ -arrestin-2 recruitment, and  
14  
15 receptor internalization.  
16  
17  
52518

19  
20  
21  
52722 **Figure 3: GRK Recruitment and  $\beta$ -arrestin-2 conformational dynamics**  
23  
24 Agonist dose-dependent data and kinetic data of maximum treatment dose of (**A-C**) GRK2 and (**D-F**) GRK3  
25  
26 recruitment to receptor as measured by a split nanoluciferase assay. Data are grouped by treatment condition.  
27  
28  
53029 Mean  $\pm$  SEM, n=3-4. (**G**) Schematic of FlAsH assay to detect  $\beta$ -arrestin-2 conformational dynamics following  
30  
31 receptor stimulation using intramolecular BRET (Lee et al., 2016). (**H**) Location of N-terminal RLuc and CCPGCC  
32  
33 FlAsH-EDT<sub>2</sub> binding motifs on  $\beta$ -arrestin-2. (**I-K**) Radar plots of FlAsH 1-6 grouped by treatment. (**L-P**) Radar  
34  
35 plots of FlAsH 1-6 grouped by receptor. Mean, n=5. For FlAsH BRET (**I-P**), data is the average of five consecutive  
36  
37 reads taken approximately 10 minutes after the addition of ligand. See S4-S5 for additional GRK recruitment  
38  
39 data and S6 for raw FlAsH data.  
40  
41  
53642  
43  
44  
53745 **Figure 4: Impact of the phosphorylation pattern on  $\beta$ -arrestin-2 conformational dynamics**  
46  
47  
53848 (**A**) Structural model of the construct used in the FlAsH BRET conformational assay. The positions of Probes 1-  
49  
50 5 are depicted as red spheres. Shown are the correlations between the distance of studied FlAsH probes to the  
51  
52 RLuc domain and the interdomain rotation angle of  $\beta$ -arrestin 2. As the RLuc domain is absent in the simulated  
53  
54 system, distance from the studied probes was approximated to a residue in the beginning of the N-terminal  
55  
56 domain (the attachment point of the RLuc), depicted as a green sphere. **B**) The  $\beta$ -arrestin 2/WT-CXCR3 C-tail  
57  
58 complex. Negatively charged residues (Asp, Glu or phosphorylated Ser and Thr) on the C-tail are depicted in  
59  
60 licorice and their C $\alpha$  atoms are highlighted with red spheres. Positions mutated within this study are labeled. The  
61  
62  
63  
64  
65

1 insert provides a detailed depiction of the lariat loop region of β-arrestin 2 (blue) and interactions with negatively  
2 charged residues of the C-tail. Bar charts demonstrate the stability of polar interactions between K294 of the  
3 lariat loop and S358 and E359 of the C-tail. Values for the WT and T360AS361A systems are colored in red. (C)  
4  
5 Density plots depicting interdomain rotation angles assumed by β-arrestin-2 during MD simulations with C-tail  
6 mutants.  
7  
8

9  
10  
11

12  
13  
14  
15 **Figure 5: Characterization of the global phosphoproteome in HEK293 cells treated with endogenous**  
16  
17 **CXCR3 agonist**

18  
19  
20 (A) HEK293 cells expressing CXCR3-WT were stimulated with vehicle control or 100 nM chemokine for five  
21 minutes. Heat map of statistically significant phosphopeptides normalized to vehicle control are shown. n=2  
22 technical replicates of six pooled biological replicates. (B) Cluster analysis of significant phosphopeptides using  
23 GProX (Rigbolt *et al.*, 2011). Cluster 0 is not shown for clarity due to low membership count. (C-E) Gene Ontology  
24 analysis of significant phosphopeptides as grouped by biological process, molecular function or cellular  
25 compartment, respectively. Percentiles demonstrate number of individual phosphopeptides present in each  
26  
27 Gene Ontology Term. (F) Manually curated, literature-based kinase enrichment analysis to predict kinase activity  
28 based on significant phosphopeptides using Kinase Enrichment Analysis 2 (Lachmann and Ma'ayan, 2009). (G)  
29 Consensus sequences of significant phosphopeptides in the dataset as generated using MoMo from MeMe suite  
30 and identified kinases with listed consensus motif based on manual literature review (Keshava Prasad *et al.*,  
31 2009). See S7 for additional global phosphoproteomic data.  
32  
33  
34  
35  
36  
37  
38  
39  
40  
41  
42  
43  
44  
45  
46

47 **Figure 6: Differential regulation of kinases by biased ligands and phosphodeficient receptors**

48  
49 Biased phosphorylation of various kinases identified from the global phosphoproteomics data including (A)  
50  
51 ERK1, (B) RAF1, (C) BRAF, (D) Casein kinase 2 (CSNK2A3/CSNK2A1), (E) Src family of protein tyrosine  
52 kinases (FYN/YES1/LCK/SRC), and (F) JNKs (JNK1/JNK3). Data is normalized to vehicle treatment and n=2  
53 technical replicates of six pooled biological replicates. Mean ± SEM. \*P<.05 by one-way ANOVA, Tukey's post  
54 hoc testing. (G) Representative western blot of phosphorylated ERK1/2 (pERK 1/2) and total ERK1/2 (tERK 1/2)  
55  
56 following stimulation with vehicle control or 100 nM of CXCL11 for five minutes. (H-J) Quantification of western  
57  
58  
59  
60 following stimulation with vehicle control or 100 nM of CXCL11 for five minutes. (H-J) Quantification of western  
61  
62  
63  
64  
65

1 blots of pERK1/2 levels at 5, 30, and 60 minutes. Mean  $\pm$  SEM, n=4. \*P<.05 by two-way ANOVA, Dunnet's post  
2 hoc testing denotes comparisons between a specific ligand/receptor combination to the same ligand at CXCR3-  
3 WT. See S8 for quantification of western blots grouped by receptor.  
4  
5  
6  
7  
8  
9  
10

576<sup>11</sup> **Figure 7: Jurkat chemotaxis and model of the phosphorylation barcode**  
577<sup>12</sup>

577<sup>13</sup> (A) Schematic of lentiviral production carrying cDNA for CXCR3-WT or one of the four receptor mutants,  
578<sup>14</sup> generation of CXCR3-KO Jurkats using CRISPR/Cas9, and creation of stably expressing CXCR3 Jurkats. (B)  
579<sup>15</sup>  
580<sup>16</sup> Surface expression of CXCR3-KO Jurkats or five various Jurkat cell lines transduced with lentivirus carrying the  
581<sup>17</sup> listed receptor cDNA as measured with flow cytometry. Dotted line denotes a fluorescence intensity of 10<sup>2</sup>. For  
582<sup>18</sup> transduced cells, cells with a fluorescence intensity greater than 10<sup>2</sup> were sorted for chemotaxis experiments.  
583<sup>19</sup>  
584<sup>20</sup> (C) Jurkat chemotaxis for each receptor/ligand combination. Mean  $\pm$  SEM, n=4. \*P<.05 by two-way ANOVA,  
585<sup>21</sup>  
586<sup>22</sup> Tukey's post hoc testing denotes comparisons between a specific ligand/receptor combination to the same ligand  
587<sup>23</sup> at CXCR3-WT. (D) Principal Component Analysis of G Protein activation and  $\beta$ -arrestin-2 recruitment versus  
588<sup>24</sup> chemotaxis. (E) Principal Component Analysis of G Protein activation,  $\beta$ -arrestin-2 recruitment, GRK2 and GRK3  
589<sup>25</sup> recruitment, and FIAsh versus chemotaxis. See S9 for chemotaxis data grouped by receptor and univariate  
590<sup>26</sup> analyses. (F) Working model for biased ligand generation of unique barcode ensembles which differentially  
591<sup>27</sup> regulate G protein signaling,  $\beta$ -arrestin recruitment and conformation, receptor endocytosis, kinase activity, the  
592<sup>28</sup> global phosphoproteome, and cellular functions such as chemotaxis.  
593  
594  
595  
596  
597  
598  
599  
600  
601  
602  
603  
604  
605  
606  
607  
608  
609  
610  
611  
612  
613  
614  
615  
616  
617  
618  
619  
620  
621  
622  
623  
624  
625  
626  
627  
628  
629  
630  
631  
632  
633  
634  
635  
636  
637  
638  
639  
640  
641  
642  
643  
644  
645  
646  
647  
648  
649  
650  
651  
652  
653  
654  
655  
656  
657  
658  
659  
660  
661  
662  
663  
664  
665

1  
590 2 **STAR Methods**  
591 3  
592 4  
593 5

594 6 **RESOURCE AVAILABILITY**  
595 7  
596 8  
597 9

598 10 **Lead Contact**  
599 11  
600 12 Further information and requests for resources and reagents should be directed to and will be fulfilled by the  
601 13 lead contact, Sudarshan Rajagopal ([Sudarshan.rajagopal@duke.edu](mailto:Sudarshan.rajagopal@duke.edu)).  
602 14  
603 15  
604 16  
605 17  
606 18

598 19 **Materials Availability**  
599 20  
600 21 All plasmids generated in this study will be distributed upon request.  
601 22  
602 23  
603 24

601 25 **Data and Code Availability**  
602 26  
603 27 The RAW MS data and the identified results from Maxquant have been deposited in Japan ProteOme STandard  
604 28 Repository (jPOST: <https://repository.jpostdb.org/>) (Watanabe et al., 2021). The accession codes: JPST001599  
605 29 for jPOST and PXD034033 for ProteomeXchange. The access link is  
606 30 <https://repository.jpostdb.org/preview/1101419412628c1a4318aa7> and access key is 6844. Molecular dynamics  
607 31 simulations have been deposited in GPCRmd (<https://submission.gpcrmd.org/dynadb/publications/1485/>) with  
608 32 the ID 1485.  
609 33  
610 34  
611 35

609 36 **EXPERIMENTAL MODEL AND SUBJECT DETAILS**  
610 37  
611 38

611 39 **Bacterial strains**  
612 40  
613 41 XL-10 Gold ultracompetent E. coli (Agilent) were used to express all constructs used in this manuscript.  
614 42  
615 43

614 44 **Cell Lines**  
615 45  
616 46 Human Embryonic Kidney (HEK293,  $\beta$ -arrestin 1/2 knockout) cells were grown in minimum essential media  
617 47 (MEM) supplemented with 10% fetal bovine serum (FBS) and 1% penicillin/streptomycin at 37°C and 5% CO<sub>2</sub>.  
618 48  
619 49  $\beta$ -arrestin 1/2 KO HEK293 cells and GRK 2/3/5/6 KO HEK293 cells were provided by Asuka Inoue and validated  
620 50  
621 51  
622 52  
623 53  
624 54  
625 55  
626 56  
627 57  
628 58  
629 59  
630 60  
631 61  
632 62  
633 63  
634 64  
635 65

1 as previously described (Alvarez-Curto et al., 2016; Pandey et al., 2021a). Jurkat cells were cultured in RPMI  
2  
3 1640 supplemented with 10% FBS and 1% penicillin/streptomycin at 37°C and 5% CO<sub>2</sub>.  
4  
5

621 9 **METHOD DETAILS**  
622 10  
623 11  
624 12  
625 13 **Cell culture and transfection**  
626 14

627 15 Human embryonic kidney cells (HEK293, GRK 2/3/5/6 knockout, β-arrestin 1/2 knockout) were maintained at  
628 16 37°C and 5% CO<sub>2</sub>, in minimum essential medium supplemented with 1% penicillin/streptomycin and 10% fetal  
629 17 bovine serum (FBS). For BRET and luminescence studies, HEK293 cells were transiently transfected via an  
630 18 optimized calcium-phosphate protocol as previously described (Pack et al., 2018). In the calcium phosphate  
631 19 transfection method, cell culture media was replaced 30 minutes prior to transfection. Plasmids were suspended  
632 20 in water, and calcium chloride was added to the plasmid constructs to a final concentration of 250 μM. An equal  
633 21 volume of 2x HEPES-buffered saline solution (10 mM D-Glucose, 40 mM HEPES, 10 mM potassium chloride,  
634 22 270 mM sodium chloride, 1.5 mM disodium hydrogen phosphate dihydrate) was added to the solution, allowed  
635 23 to incubate for two minutes, and subsequently added to the cells. For mass spectrometry studies and confocal  
636 24 microscopy, constructs were overexpressed in HEK293 cells using FuGENE 6 according to the manufacturer's  
637 25 instructions (Promega, Madison, WI). For TGF-α shedding assay cells, were transiently transfected using  
638 26 Lipofectamine 2000 according to the manufacturer's instructions (Thermo Fisher Scientific).  
639 27  
640 28  
641 29

642 30 **Generation of constructs**  
643 31  
644 32

645 33 Cloning of constructs was performed using conventional techniques such as restriction enzyme and ligation  
646 34 methods. CXCR3 C-terminal phosphomutant constructs were generated using a QuikChange Lightening  
647 35 Mutagenesis Kit (Agilent, Santa Clara, CA). Linkers between the fluorescent proteins or luciferases and the  
648 36 cDNAs for receptors, transducers, kinases, or other proteins were flexible and ranged between 2 and 17 amino  
649 37 acids.  
650  
651

652 **Cell lysis and protein extractions**  
653  
654  
655

1  
645 2 For protein extraction, cell pellets were resuspended in cell lysis buffer (100 mM NH<sub>4</sub>HCO<sub>3</sub>, pH 8.0, 8 M urea,  
3  
646 4 75 mM sodium chloride (NaCl), 10 mM sodium fluoride (NaF), 1% phosphatase inhibitor cocktail 2 (Sigma P  
5  
647 6 5726), 1% phosphatase inhibitor cocktail 3 (Sigma P 0044), pH 8.0) and sonicated in an ice-bath for 3 mins  
7  
648 8 followed by homogenization using a hand-held SpiralPestle™ and MicroTube Homogenizer (BioSpec products,  
9  
10  
649 11 Bartlesville, OK) on ice until complete visual homogenization was achieved. Cell lysates were centrifuged, and  
12  
650 13 the protein concentrations were measured with a Pierce BCA protein assay (Thermo Fisher Scientific). Proteins  
14  
651 15 were reduced with 5 mM dithiothreitol for one hour at 37°C and subsequently alkylated with 20 mM  
16  
652 17 iodoacetamide for one hour at 25°C in the dark. Samples were diluted 1:8 with 50 mM NH<sub>4</sub>HCO<sub>3</sub> and digested  
18  
653 19 with sequencing-grade modified trypsin (Promega, V5117) at a 1:50 enzyme-to-substrate ratio. After three hours  
20  
654 21 of digestion at 37°C, the digested samples were acidified with 100% formic acid (FA) to 1% of the final  
22  
655 23 concentration of FA and centrifuged for 15 minutes at 1,500 ×g at 4°C before transferring samples into new tubes  
24  
656 25 leaving the resulting pellet behind. Digested samples were desalted using a 4-probe positive pressure Gilson  
26  
657 27 GX-274 ASPEC™ system (Gilson Inc., Middleton, WI) with Discovery C18 100 mg/1 mL solid phase extraction  
28  
658 29 tubes (Supelco, St.Louis, MO), using the following protocol: 3 mL of methanol was added for conditioning  
30  
659 31 tubes (Supelco, St.Louis, MO), using the following protocol: 3 mL of methanol was added for conditioning  
32  
660 33 followed by 2 mL of 0.1% trifluoroacetic acid (TFA) in H<sub>2</sub>O. The samples were then loaded onto each column  
35  
661 36 followed by 4mL of 95:5: H<sub>2</sub>O:acetonitrile (ACN), 0.1% TFA. Samples were eluted with 1mL 80:20 ACN:H<sub>2</sub>O,  
37  
662 38 0.1% TFA. The samples were completely dried using a SpeedVac vacuum concentrator.  
39  
663 40  
664 41  
665 42 **TMT-10 labeling of peptides**  
43  
666 44 The dried tryptic peptides were dissolved with 500 mM HEPES (pH 8.5) and then labeled with 10-plex Tandem  
45  
667 46 Mass Tag™ (TMT) reagents (Thermo Fisher Scientific) in 100% ACN. A ratio of TMT to peptide amount of 10:1  
47  
668 48 (w/w) was used (i.e., 500 µg of peptides labeled by 5 mg of TMT reagent). After incubation for one hour at room  
49  
669 50 temperature, the reaction was terminated by adding 5% hydroxylamine for 15 minutes at room temperature. The  
51  
670 52 TMT-labeled peptides were then acidified with 0.5% FA. Peptides labeled by different TMT reagents were then  
53  
671 54 mixed, dried using a SpeedVac vacuum concentrator, reconstituted with 3% ACN, 0.1% FA and desalted again  
55  
672 56 with C18 SPE.  
57  
673 58  
674 59  
675 60  
676 61  
677 62  
678 63  
679 64  
680 65

1  
672 **Peptide fractionation and enrichment**  
2  
3

4 The peptides were further fractionated using a reversed-phase Waters XBridge C18 column (250 mm × 4.6 mm  
5 column packed with 3.5-μm particles) on an Agilent 1200 HPLC System (solvent A: 5 mM ammonium formate,  
6 pH 10, 2% ACN; solvent B: 5 mM ammonium formate, pH 10, 90% ACN) operating at a flow rate of 1 mL/min  
7 [Anal. Chem. 2019, 91, 9, 5794–5801]. Peptides were separated by a gradient mixture from 0% B to 16% B in  
8 six minutes, 40% B in 60 minutes, 44% B in 4 min and ramped to 60% B in five minutes. The 60% B mixture was  
9 kept for 14 min. Fractions were collected into a 96 well plate during the fractionation run with a total of 96 fractions  
10 at the 1-minute time interval. The 96 fractions were subsequently concatenated into 24 fractions by combining 4  
11 fractions that are 24 fractions apart (i.e., combining fractions #1, #25, #49, and #73; #2, #26, #50, and #74; and  
12 so on). For proteome analysis, 5% of each concatenated fraction was dried down and re-suspended in 2%  
13 acetonitrile, 0.1% formic acid to a peptide concentration of 0.1 mg/mL for LC-MS/MS analysis. The rest of the  
14 fractions (95%) were further concatenated into 12 fractions (i.e., by combining fractions #1 and #13; #3 and #15;  
15 and so on), dried down, and phosphopeptides enriched using immobilized metal affinity chromatography (IMAC).  
16  
17

18  
685 **Phosphopeptide enrichment using IMAC**  
19  
20

21 The procedure for IMAC phosphopeptide enrichment has previously been reported here (Mertins et al., 2018).  
22 Briefly, Fe<sup>3+</sup>-NTA-agarose beads were freshly prepared using the Ni-NTA Superflow agarose beads (QIAGEN,  
23 #30410) for phosphopeptide enrichment. For each of the 12 fractions, peptides were reconstituted in 500 μL  
24 IMAC binding/wash buffer (80% ACN, 0.1% TFA) and incubated with 20 μL of the 50% bead suspension for 30  
25 minutes at RT. After incubation, the beads were sequentially washed with 50 μL of the wash buffer (1X), 50 μL  
26 of 50% ACN, 0.1% TFA (1X), 50 μL of the wash buffer (1X), and 50 μL of 1% FA (1X) on the stage tip packed  
27 with 2 discs of Empore C18 material (Empore Octadecyl C18, 47 mm; Supelco, 66883-U). Phosphopeptides  
28 were eluted from the beads onto the C18 disc using 70 μL of the elution buffer (500 mM K<sub>2</sub>HPO<sub>4</sub>, pH 7.0). Sixty  
29 microliters of 50% ACN, 0.1% FA was used for the elution of phosphopeptides from the C18 stage tips after two  
30 washes with 100 μL of 1% FA. Samples were dried using a Speed-Vac and later reconstituted with 12 μL of 3%  
31 ACN, 0.1% FA for LC-MS/MS analysis.  
32  
33

34  
698  
35  
699  
36  
700  
37  
701  
38  
702  
39  
703  
40  
704  
41  
705  
42  
706  
43  
707  
44  
708  
45  
709  
46  
710  
47  
711  
48  
712  
49  
713  
50  
714  
51  
715  
52  
716  
53  
717  
54  
718  
55  
719  
56  
720  
57  
721  
58  
722  
59  
723  
60  
724  
61  
725  
62  
726  
63  
727  
64  
728  
65

1  
2 **LC-MS/MS Analysis**  
3

4 Lyophilized global and phosphorylated peptides were reconstituted in 12 µL of 0.1% FA with 2% ACN and 5 µL  
5 of the resulting sample was analyzed by LC-MS/MS using a Q-Exactive HF Quadrupole-Orbitrap Mass  
6 Spectrometer (Thermo Scientific) connected to a nanoACQUITY UPLC system (Waters Corp., Milford, MA)  
7 (buffer A: 0.1% FA with 3% ACN and buffer B: 0.1% FA in 90% ACN) as previously described (Tsai et al., 2020).  
8  
9 Peptides were separated by a gradient mixture with an analytical column (75 µm i.d. × 25 cm) packed using 1.9-  
10 µm ReproSil C18 and with a column heater set at 50 °C. The analytical column was equilibrated to 98% buffer  
11 A and 2% buffer B and maintained at a constant column flow of 200 nL/min. Data were acquired in a data  
12 dependent mode with a full MS scan (350-1800 m/z) at a resolution of 60K with AGC setting set to  $4 \times 10^5$ . The  
13 isolation window (quadrupole) for MS/MS was set at 0.7 m/z and optimal HCD fragmentation was performed at  
14 a normalized collision energy of 30% with AGC set as  $1 \times 10^5$  and a maximum ion injection time of 105 ms. The  
15 MS/MS spectra were acquired at a resolution of 50K. The dynamic exclusion time was set at 45 s.  
16  
17

18  
19  
20  
21  
22  
23  
24  
25  
26  
27 **MS Data Analysis**  
28  
29  
30

31 The raw MS/MS data were processed with MaxQuant (Cox and Mann, 2008; Tyanova et al., 2016a). The MS/MS  
32 spectra were searched against a human UniProt database (fasta file dated April 12, 2017 with 20,198  
33 sequences). The search type was set to “Reporter ion MS2” for isobaric label measurements. A peptide search  
34 was performed with full tryptic digestion (Trypsin) and allowed a maximum of two missed cleavages.  
35 Carbamidomethyl (C) was set as a fixed modification; acetylation (protein N-term) and oxidation (M) were set as  
36 variable modifications for global proteome analysis. Acetylation (protein N-term), oxidation (M) and Phospho  
37 (STY) were set as variable modifications for phosphoproteome analysis. The false discovery rate (FDR) was set  
38 to 1% at the level of proteins, peptides, and modifications; no additional filtering was performed. The intensities  
39 of all ten TMT reporter ions were extracted from MaxQuant outputs and the abundances of TMT were firstly log2  
40 transformed. The phosphoproteome data were further processed by the Ascore algorithm (Beausoleil et al.,  
41 2006) for phosphorylation site localization, and the top-scoring sequences were reported. The Perseus (Tyanova  
42 et al., 2016b) was used for statistical analyses.  
43  
44  
45  
46  
47  
48  
49  
50  
51  
52  
53  
54  
55  
56  
57  
58  
59  
60  
61  
62  
63  
64  
65

1  
2 **Flow cytometry and fluorescence-activated cell sorting (FACS)**  
3

4 Flow cytometry was utilized to assess wild-type CXCR3 and CXCR3 mutant receptor cell surface expression in  
5 HEK293 cells. HEK293 cells seeded in six-well plates were transfected with wild-type CXCR3 or the indicated  
6 CXCR3 mutant using the calcium phosphate method. Forty-eight hours later, the cells were collected, washed  
7 with ice cold phosphate buffered saline (PBS), and subsequently centrifuged at 600 g for 4 minutes at 4 °C.  
8  
9 Supernatant was aspirated and cells were resuspended in ice cold PBS and counted. 1E6 cells were transferred  
10 to a new tube and resuspended in 100 µL of blocking buffer (PBS + 3% FBS + 10mM EDTA + 5% Normal Human  
11 Serum) on ice for 5 to 10 minutes. PE conjugated anti-Human CD183 (CXCR3) antibody (R&D Systems,  
12 Minneapolis, MN) was added per the manufacturers guidelines and cells were incubated for 20 to 30 minutes at  
13 room temperature in the dark. Cells were centrifuged once more, supernatant aspirated, and fixed in 300 µL of  
14 0.4% paraformaldehyde and were assessed using a BD LSRII flow cytometer. Flow cytometry was performed in  
15 the Duke Human Vaccine Institute Research Flow Cytometry Facility (Durham, NC). FACS was utilized to select  
16 Jurkat cells expressing wild-type CXCR3 or the indicated CXCR3 mutant. Following lentiviral transduction and  
17 subsequent puromycin selection, Jurkat cells were collected and washed in Hank's Balanced Salt Solution  
18 (HBSS) (Gibco) with 2.5% FBS and 1.5 µM EDTA. Cells were then labelled with APC conjugated anti-Human  
19 CD183 (CXCR3) antibody (Biolegend, San Diego, CA) for 25 minutes on ice in the dark. Cells were then washed  
20 with HBSS with 2.5% FBS and 1.5 µM EDTA and resuspended with DNase. Cells were then strained through a  
21 sterile 30 µm filter and sorted on an Astrios (Beckman Coulter) sorter. Analyses were conducted with FlowJo  
22 version 10 software.  
23  
24  
25  
26

27 **TGF- $\alpha$  shedding assay**  
28

29 G protein activity of various CXCR3 phosphorylation deficient mutants was assessed by the TGF- $\alpha$  shedding  
30 assay as previously described (Inoue et al., 2012). HEK293 cells were transiently transfected using  
31 Lipofectamine 2000 (Thermo Fisher Scientific) with wild-type CXCR3 or the indicated CXCR3 mutant receptor,  
32 modified TGF- $\alpha$ -containing alkaline phosphatase (AP-TGF- $\alpha$ ), and the Gai1 or Gai3 subunit or the negative  
33 control GaΔc. 24 hours later, cells were detached and reseeded in HBSS with 5 mM HEPES in a clear-bottomed,  
34 white-walled, Costar 96-well plate (Corning Inc., Corning, NY). One hour later, cells were stimulated with the  
35  
36  
37  
38  
39  
40  
41  
42  
43  
44  
45  
46  
47  
48  
49  
50  
51  
52  
53  
54  
55  
56  
57  
58  
59  
60  
61  
62  
63  
64  
65

1 indicated concentration of CXCL11 for one hour. Conditioned medium (CM) containing the shed AP-TGF- $\alpha$  was  
2 transferred to a new 96-well plate. Both the cells and CM were treated with para-nitrophenylphosphate (p-NPP,  
3 100 mM; Sigma-Aldrich, St. Louis, MO) substrate for one hour. The conversion of p-NPP to para-nitrophenol (p-  
4 NP) was measured at an optical density at 405 nm ( $OD_{405}$ ) in a BioTek Synergy Neo2 plate reader plate reader  
5 immediately after p-NPP addition and then after a 1-hour incubation. G $\alpha$  activity was calculated by determining  
6 p-NP amounts by absorbance using the following equation:  
7  
8

$$100 * \left( \frac{\Delta OD_{405,CM}}{\Delta OD_{405,CM} + \Delta OD_{405,Cell}} \right)$$

9 where  $\Delta OD_{405} = OD_{405 \text{ at } 1\text{hr}} - OD_{405 \text{ at } 0 \text{ hours}}$  and  $\Delta OD_{405, \text{cell}}$  and  $\Delta OD_{405, \text{CM}}$  represent the changes in absorbance  
10 after one hour in the cell and CM plates, respectively. Data were normalized to the negative control G $\alpha$  $\Delta$ c.  
11  
12

## 13 762 Split luciferase and BRET assays

14  
15

16 HEK293 cells seeded in six-well plates (~750000 cells/well) were transfected with the appropriate constructs  
17 using the calcium-phosphate protocol. TRUPATH assays to assess G protein dissociation utilized wild-type  
18 CXCR3 or the indicated CXCR3 mutant, Gai1-RLuc8, Gy9-GFP2, and G $\beta$ 3 at equal amounts (Olsen *et al.*,  
19 2020).  $\beta$ -arrestin-2 recruitment was assessed using wild-type CXCR3 or the indicated CXCR3 mutant tagged  
20 with a C-terminal RLuc2 and a  $\beta$ -arrestin-2-mKO. Receptor internalization was assessed using wild-type CXCR3  
21 or the indicated CXCR3 mutant tagged with a C-terminal RLuc2 and either a Myrpalm tagged mVenus to assess  
22 proximity to the cellular membrane, or a 2x-Fyve tagged mVenus to assess proximity to the early endosome.  
23  
24 GRK recruitment was assessed using a split luciferase assay where wild-type CXCR3 or the indicated CXCR3  
25 mutant was tagged with a SmBiT and GRK2, GRK3, GRK5, or GRK6 was tagged with a LgBiT.  
26  
27

28 Twenty-four hours after transfection, cells were washed with PBS, collected with trypsin, and plated onto clear-  
29 bottomed, white-walled, Costar 96-well plates at 50000 to 100000 cells/well in BRET medium (clear minimum  
30 essential medium (Gibco) supplemented with 2% fetal bovine serum, 10 mM HEPES, 1x GlutaMax (Gibco), and  
31 1x Antibiotic-Antimycotic (Gibco)). The following day, media was removed, and cells were incubated at 37°C with  
32 80  $\mu$ L of HBSS supplemented with 20 mM HEPES and 3  $\mu$ M coelenterazine-400a (Cayman Chemical, Ann Arbor,  
33 MI) for TRUPATH or 3  $\mu$ M coelenterazine h for all other BRET or split luciferase assays (Cayman Chemical, Ann  
34 Arbor, MI) for 10 to 15 minutes. For TRUPATH, plates were read with a BioTek Synergy Neo2 plate reader set  
35 63 64 65

1 at 37°C with a standard 400 nm emission filter and 510 nm long pass filter. For all other BRET assays, a standard  
2 3  
3 4 480 nm RLuc emission filter and 530 nm (for experiment using mVenus) or custom 542 nm (for experiments  
4 5 using mKO) long pass filter was utilized (Chroma Technology Co., Bellows Falls, VT). Cells were stimulated with  
5 6  
6 7 either vehicle control (HBSS with 20 mM HEPES) or the indicated concentration of chemokine. All readings were  
7 8  
8 9 performed using a kinetic protocol. For split luciferase experiments, plates were read before and after ligand  
9 10  
10 11 treatment to calculate a change in luminescence after ligand stimulation and subsequently normalized to vehicle  
11 12  
12 13 treatment. For BRET experiments, the BRET ratio was calculated by dividing the acceptor signal by the luciferase  
13 14  
14 15 signal. and a net BRET ratio was calculated by normalizing to vehicle treatment.  
15 16  
16 17  
17 18  
18 19  
19 20  
20 21  
21 22 **Intramolecular Fluorescent Arsenical Hairpin (FIAsH) BRET of β-arrestin-2**  
22 23  
23 24 FIAsH BRET experiments were carried out using a modified protocol as previously described (Lee *et al.*, 2016;  
24 25  
25 26 Strungs *et al.*, 2019). FIAsH 3 serves as a negative control as insertion of the CCPGCC motif at this location  
26 27 significantly impacts β-arrestin recruitment to the receptor and does not demonstrate significant changes in  
27 28  
28 29 BRET efficiency following ligand stimulation. HEK293 cells seeded in six-well plates were transfected with wild-  
29 30 type CXCR3 or the indicated CXCR3 mutant and FIAsH 1, 2, 3, 4, 5, or 6 using the calcium-phosphate protocol.  
30 31  
31 32 Twenty-four hours after transfection, cells were washed with PBS, collected with trypsin, and plated onto clear-  
32 33  
33 34 bottomed, rat-tail collagen coated, white-walled, Costar 96-well plates at 50000 to 100000 cells/well in  
34 35  
35 36 supplemented MEM. The following day, cells were washed with 50 µL of HBSS and incubated in biarsenical  
36 37  
37 38 labelling reagent FIAsH-EDT2 at a final concentration of 2.5 µM for 45 minutes at room temperature in the dark.  
38 39  
39 40 Cells were then washed once with a 250 µM BAL wash buffer (2,3-dimercaptopropanol) and incubated with  
40 41  
41 42 HBSS with 20 mM HEPES. Cells were stimulated by either vehicle control (HBSS with 20 mM HEPES) or  
42 43  
43 44 chemokine for eight minutes. Immediately before reading the plate, cells were treated with coelenterazine h and  
44 45  
45 46 read on a BioTek Synergy Neo2 plate reader set at 37°C using standard 480 nm and 530 nm emission filters.  
46 47  
47 48 Net BRET values were calculated as described by averaging six consecutive BRET values and normalizing to  
48 49  
49 50 vehicle control. Two-way ANOVA was performed at each FIAsH construct to determine if there was a significant  
50 51  
51 52 ligand, receptor, or interaction term. If a significant interaction term was detected, Tukey's post hoc testing was  
52 53  
53 54 performed for multiple comparisons between receptor:ligand combinations at the specified FIAsH construct.  
54 55  
55 56  
56 57  
57 58  
58 59  
59 60  
60 61  
61 62  
62 63  
63 64  
64 65

1  
2  
3  
4  
5  
6

808 4 **Molecular Dynamics**  
809 5

810 6 The model of the CXCR3 C-tail/  $\beta$ -arrestin 2 complex was based on the structure of  $\beta$ -arrestin 1 in complex with  
811 7 the V2R C-tail (Shukla *et al.*, 2013). The sequence of  $\beta$ -arrestin 2 was modified to match the isoform used in the  
812 8 FIAsH *in vitro* experiments [P29067]. The complexes were solvated (TIP3P water) and neutralized using a 0.15  
813 9 M concentration of NaCl ions. Parameters for simulations were obtained from the Charmm36M forcefield (Huang  
814 10 et al., 2017). Simulations were run using the ACEMD3 engine (Harvey *et al.*, 2009). All systems underwent a  
815 11 40ns equilibration in conditions of constant pressure (NPT ensemble, pressure maintained with Berendsen  
816 12 barostat, 1.01325 bar), using a timestep of 2fs. During this stage mobility restraints were applied to the backbone.  
817 13 This was followed with 3 x 1.5 $\mu$ s of simulation for each system in conditions of constant volume (NVT ensemble)  
818 14 using a timestep of 4fs. For every simulation we used a temperature of 310K, maintained using the Langevin  
819 15 thermostat. Hydrogen bonds were restrained using the RATTLE algorithm. Non-bonded interactions were cut-  
820 16 off at a distance of 9 $\text{\AA}$ , with a smooth switching function applied at 7.5 $\text{\AA}$ . The interdomain rotation angle of  $\beta$ -  
821 17 arrestin 2 was analyzed using a script kindly provided by Naomi Latoracca (Latorraca *et al.*, 2018). The angle  
822 18 was measured by comparing the displacement of the C-domain relative to the N-domain between the inactive  
823 19 (PDB code: 1G4R) and active  $\beta$ arr1 crystal structures (PDB code: 4JQI). Each simulation frame was aligned to  
824 20 the reference structures using the Ca atoms of the  $\beta$ -strands present within the N-domain, while the same atoms  
825 21 present in the C-domain were used to calculate the rotation angle. For each of the variants of the C-tail, we have  
826 22 phosphorylated all Ser and Thr residues present within the sequence. To study correlation of the interdomain  
827 23 rotation angle, and the distance between the studied probes and Arg8 (RLuc anchor point), we have utilized  
828 24 simulations of the L344X system (which in our setup meant that a C-tail was not included at all). Simulation data  
829 25 are shared on the open online resource GPCRmd (Rodriguez-Espigares *et al.*, 2020) with the ID 1485.  
830 26  
831 27

830 28 53 **Immunoblotting**  
831 29 54

832 30 Experiments were conducted as previously described (Smith *et al.*, 2018b). Briefly, HEK293 cells were  
833 31 transiently transfected via the calcium-phosphate method with either wild-type CXCR3 or the indicated CXCR3  
834 32 mutant. 48 hours after transfection, the cells were serum starved in minimum essential medium with 1%  
835 33  
836 34  
837 35  
838 36  
839 37  
840 38  
841 39  
842 40  
843 41  
844 42  
845 43  
846 44  
847 45  
848 46  
849 47  
850 48  
851 49  
852 50  
853 51  
854 52  
855 53  
856 54  
857 55  
858 56  
859 57  
860 58  
861 59  
862 60  
863 61  
864 62  
865 63  
866 64  
867 65

1 penicillin/streptomycin, 0.05% bovine serum albumin, and 5 mM HEPES for at least four hours, stimulated to a  
2 final concentration with 100 nM chemokine or vehicle control for 5, 30 or 60 minutes, subsequently washed once  
3 with ice-cold PBS, lysed in ice-cold radioimmunoprecipitation assay buffer (150 mM NaCl, 1% Nonidet P-40,  
4 0.5% sodium deoxycholate, 0.1% sodium dodecyl sulfate (SDS), 25 mM Tris pH 7.4) containing the phosphatase  
5 inhibitor PhosSTOP (Roche, Basel, Switzerland) and protease inhibitor cOmplete EDTA free (Sigma-Aldrich, St.  
6 Louis, MO). Samples were then rotated for approximately 45 minutes at 4 °C and cleared of insoluble debris by  
7 centrifugation at 17000 g at 4 °C for 15 minutes, after which the supernatant was collected. Protein was resolved  
8 on SDS-10% polyacrylamide gels, transferred to nitrocellulose membranes, and immunoblotted with the  
9 indicated primary antibody overnight at 4 °C. phospho-ERK (Cell Signaling Technology) and total ERK (Millipore)  
10 were used to assess ERK activation. Peroxidase-conjugated polyclonal donkey anti-rabbit immunoglobulin (IgG)  
11 or polyclonal sheep anti-mouse IgG were used as secondary antibodies. Immune complexes on nitrocellulose  
12 membrane were imaged by SuperSignal enhanced chemiluminescent substrate (Thermo Fisher) using a  
13 ChemiDoc MP Imaging System (Bio-Rad). For quantification, phospho-ERK signal was normalized to total ERK  
14 signal using ImageLab (Bio-Rad) within the same immunoblot.  
15  
16

### 848<sup>33</sup> 849<sup>34</sup> 850<sup>35</sup> **Confocal microscopy**

851<sup>36</sup> HEK293 cells plated in rat-tail-collagen-coated 35 mm glass bottomed dishes (MatTek Corporation, Ashland,  
852<sup>37</sup> MA) were transiently transfected using FuGENE 6 with either wild-type CXCR3-GFP or the indicated CXCR3-  
853<sup>38</sup> GFP mutant and β-arrestin-2-RFP. 48 hours after transfection, the cells were serum starved for one hour prior  
854<sup>39</sup> to treatment with the indicated chemokine at 100 nM for 45 minutes at 37°C. The samples were then washed  
855<sup>40</sup> once with HBSS and fixed in a 6% formaldehyde solution for 30 minutes in the dark at room temperature. Cells  
856<sup>41</sup> were then washed four times with PBS and subsequently imaged with a Zeiss CSU-X1 spinning disk confocal  
857<sup>42</sup> microscope using the corresponding lasers to excite GFP (480 nm) and RFP (561 nm). Confocal images were  
858<sup>43</sup> arranged and analyzed using ImageJ (NIH, Bethesda, MD).  
859<sup>44</sup>  
860<sup>45</sup>

### 861<sup>46</sup> **Generation of stably expressing CXCR3 Jurkats and Jurkat Chemotaxis**

862<sup>47</sup>  
863<sup>48</sup>  
864<sup>49</sup>  
865<sup>50</sup>

1 CXCR3 knock out (CXCR3-KO) Jurkat cells were generated using CRISPR-Cas9. CXCR3 guide RNA was  
2 developed using GAGTGACCACCAAGTGCTAAATGACG and GATGAAGTCTGGGAGGGCGAAA  
3 and inserted into a Cas9 containing plasmid backbone (PX459). Jurkat cells were transfected using  
4 Lipofectamine 2000 with the designed PX459 plasmid and CXCR3-KO Jurkats were selected using Puromycin  
5 and single clones were selected via limited dilution. CXCR3-KO was confirmed via flow cytometry. Stably  
6 expressing CXCR3 Jurkats were generated using lentiviral transduction. The wild-type or mutant CXCR3 were  
7 cloned into a pLenti plasmid backbone consisting of the receptor underneath a CMV promoter. HEK293 cells  
8 were transfected using calcium-phosphate with the pLenti receptor containing plasmid, envelope  
9 vector (pMD2.G), and packaging vector (psPAX2). 16 hours post-transfection, the HEK293 cell media was  
10 changed. 64 hours post transfection, the viral containing media was harvested, and virus was concentrated using  
11 the Lenti-X concentrator (Takara Bio, Japan) and viral titer was determined using qPCR per the manufacturer  
12 guidelines (ABM, Canada). CXCR3-KO Jurkats were transduced with virus via centrifugation at 1000 g for 90  
13 minutes at a multiplicity of infection of 80-100 in the presence of polybrene at 8 $\mu$ g/mL. Cells expressing CXCR3  
14 were sorted via FACS to obtain cells that express receptor to a similar degree. Chemotaxis assays were run in  
15 a 96 well format using the 5  $\mu$ m ChemoTx chemotaxis system (Neuro Probe, Gaithersburg, MD). 750000 Jurkats  
16 were serum starved for at least four hours and placed in the chemotaxis system and allowed to migrate towards  
17 vehicle control or chemokine. Chemotaxis was measured using a previously described MTT labeling assay  
18 where the number of migrated cells is quantified by the reduction of MTT (Shi et al., 1993). Following chemotaxis,  
19 cells were labelled with a 0.5 mg/mL solution of MTT for four hours at 37 °C, subsequently lysed in 2 mM  
20 hydrochloric acid in isopropanol, and absorbance was read at an optical density of 570 nm. Chemotactic index  
21 was determined by measuring the absorbance of cells treated with chemokine to those treated with vehicle and  
22 normalized to the cell type with maximum chemotactic response.

## 23 24 25 26 27 28 29 30 31 32 33 34 35 36 37 38 39 40 41 42 43 44 45 46 47 48 49 50 51 52 53 54 55 56 57 58 59 60 61 62 63 64 65 **Chemokines**

Recombinant Human CXCL9, CXCL10, and CXCL11 (PeproTech) were diluted according to the manufacturer's  
specifications, and aliquots were stored at -80 °C until needed for use.

1  
2 **QUANTIFICATION AND STATISTICAL ANALYSIS**  
3

4 **Statistical analyses**  
5

6 Data were analyzed in Excel (Microsoft, Redmond, WA) and graphed in Prism 9.0 (GraphPad, San Diego, CA).  
7  
8 Dose-response curves were fitted to a log agonist versus stimulus with three parameters (span, baseline, and  
9 EC50) with the minimum baseline corrected to zero. For comparing ligands or receptors in concentration-  
10 response assays, a two-way ANOVA of ligand and concentration was conducted. Unless otherwise noted,  
11 statistical tests were two-sided and Tukey's post hoc testing was performed for multiple comparisons or Dunnet's  
12 testing was performed when comparisons were made to a reference condition. Statistical significance was shown  
13 on figures typically for the  $E_{max}$  of dose-response curves. In some cases, when applicable, statistical significance  
14 was shown on figures for EC<sub>50</sub>. Unless otherwise state, post hoc comparisons were made between CXCR3-WT  
15 and the denoted phosphorylation deficient receptor. Further details of statistical analysis and replicates are  
16 included in the figure captions. Experiments were not randomized, and investigators were not blinded to  
17 treatment conditions. Critical plate-based experiments were independently replicated by at least two different  
18 investigators when feasible.  
19  
20  
21  
22  
23  
24  
25  
26  
27  
28  
29  
30  
31  
32

33  
34  
35  
36  
37  
38  
39  
40  
41  
42  
43  
44  
45  
46  
47  
48  
49  
50  
51  
52  
53  
54  
55  
56  
57  
58  
59  
60  
61  
62  
63  
64  
65

902 1 KEY RESOURCES TABLE  
2  
3

4 REAGENT OR RESOURCE	5 SOURCE	6 IDENTIFIER
<b>Antibodies</b>		
7 Donkey polyclonal anti-rabbit IgG 8 peroxidase conjugated	Rockland	Cat#611-7302; RRID:AB_219747
9 Sheep polyclonal anti-mouse IgG 10 peroxidase conjugated	Rockland	Cat#610-603-002; RRID:AB_219694
11 Mouse monoclonal anti-phospho- 12 p44/42 MAPK 1/2 (ERK1/2) 13 (Thr202/Tyr204)	Cell Signaling Technologies	Cat#9106; RRID:AB_331768
14 Rabbit polyclonal anti-MAPK 1/2 15 (ERK1/2)	Millipore Sigma	Cat#06-182; RRID:AB_310068
16 Mouse monoclonal anti-human 17 CD183 (CXCR3) PE conjugated	R&D Systems	Cat#FAB160P; RRID:AB_2086755
18 Mouse monoclonal anti-human 19 CD183 (CXCR3) APC conjugated	BioLegend	Cat#353707; RRID:AB_10962949
<b>Bacterial Strains</b>		
24 XL10-Gold Ultracompetent E. Coli	Agilent	Cat#200315
<b>Chemicals, peptides, and recombinant proteins</b>		
26 Recombinant Human CXCL9	Peprotech	Cat#300-26
27 Recombinant Human CXCL10	Peprotech	Cat#300-12
28 Recombinant Human CXCL11	Peprotech	Cat#300-46
30 GlutaMax	Gibco	Cat#35050061
31 Antibiotic-Antimycotic	Gibco	Cat#15240062
32 Fugene 6	Promega	Cat#E2691
33 Lipofectamine 2000	Invitrogen	Cat#11668019
34 para-Nitrophenyl Phosphate	Sigma-Aldrich	Cat#4876
35 2,3-dimercapto-1-propanol	Sigma-Aldrich	Cat#64046
37 FlAsH-EDT2	Santa Cruz Biotechnology	Cat#sc-363644
38 Coelenterazine h	Cayman Chemical	Cat#16894
39 Coelenterazine h	NanoLight Technology	Cat#301
40 Coelenterazine 400a	Cayman Chemical	Cat#16157
41 PhosSTOP	Sigma-Aldrich	Cat#4906845001
42 cOmplete Protease Inhibitor 43 Cocktail	Sigma-Aldrich	Cat#11697498001
45 SuperSignal West Pico PLUS 46 Chemiluminescent Substrate	Thermo Fischer Scientific	Cat#34580
47 Lenti-X Concentrator	Takara Bio	Cat#631232
48 Polybrene	Sigma-Aldrich	Cat#TR-1003
<b>Critical commercial assays</b>		
51 qPCR Lentivirus Titration Kit	Applied Biological Materials (ABM)	Cat#LV900
53 QuikChange Lightning Site- 54 Directed Mutagenesis Kit	Agilent	Cat#210518
55 ChemoTx 5 µm Chemotaxis 56 System	Neuroprobe	Cat#116-5
<b>Mass Spectrometry Resources</b>		
59 Ni-NTA Superflow Agarose Beads	Qiagen	Cat#30410
61 BCA Protein Assay Kit	ThermoFisher Scientific	Cat#A53225
62 TMT-11 reagent kit	ThermoFisher Scientific	Cat#A34808

1	Trypsin	Promega	Cat#V5117
2	Empore Octadecyl C18, 47 mm	Supleco	Cat#66883-U
3	Waters tC18 SepPak	Waters	Cat#WAT054925
4	<b>Deposited Data</b>		
5	Mass Spectrometry Proteomics Data	JPOST	JPST001599 (Accession Key 6844)
6	<b>Molecular Dynamics Simulations</b>		1485
7	<b>Experimental Models: Cell Lines</b>		
8	Human: 293	ATCC	Cat#CRL-1573; RRID:CVCL_0045
9	Human: 293	ATCC	Cat#CRL-3216; RRID:CVCL_0063
10	Human: 293 $\beta$ -arrestin 1/2 Knock Out	Asuka Inoue	(Alvarez-Curto <i>et al.</i> , 2016)
11	Human: 293 GRK 2, 3, 5, 6 Knock Out	Asuka Inoue	(Pandey <i>et al.</i> , 2021b)
12	Human: Jurkat, Clone E6-1	ATCC	Cat#TIB-152; RRID:CVCL_0367
13	<b>Recombinant DNA</b>		
14	CXCR3	Rajagopal Lab	N/A
15	CXCR3-S355A/S356A	This work	N/A
16	CXCR3-T360A/S361A/	This work	N/A
17	CXCR3- T360A/S361A/S364A/S366A	Rajagopal Lab (Smith <i>et al.</i> , 2021)	N/A
18	CXCR3-L344X	Rajagopal Lab (Smith <i>et al.</i> , 2017)	N/A
19	Gai1-RLuc8	Bryan Roth Lab (Olsen <i>et al.</i> , 2020)	N/A
20	G $\gamma$ 9-GFP2	Bryan Roth Lab (Olsen <i>et al.</i> , 2020)	N/A
21	G $\beta$ 3	Bryan Roth Lab (Olsen <i>et al.</i> , 2020)	N/A
22	CXCR3-RlucII	This work	N/A
23	CXCR3- S355A/S356A -RlucII	This work	N/A
24	CXCR3-T360A/S361A/-RlucII	This work	N/A
25	CXCR3- T360A/S361A/S364A/S366A- RlucII	This work	N/A
26	CXCR3-L344X-RlucII	This work	N/A
27	$\beta$ arr2-mKO	Rajagopal Lab (Smith <i>et al.</i> , 2021)	N/A
28	Myrpalm-mVenus	Rajagopal Lab (Smith <i>et al.</i> , 2017)	N/A
29	2x-Fyve-mvenus	Rajagopal Lab (Smith <i>et al.</i> , 2017)	N/A
30	CXCR3-GFP	Rajagopal Lab (Smith <i>et al.</i> , 2017)	N/A
31	CXCR3- S355A/S356A -GFP	This work	N/A
32	CXCR3-T360A/S361A-/GFP	This work	N/A
33	CXCR3- T360A/S361A/S364A/S366A- GFP	This work	N/A
34	CXCR3-L344X-GFP	This work	N/A
35	$\beta$ arr2-RFP	Marc Caron Lab	N/A
36	$\beta$ arr2-FIASH biosensors 1-6	Louis Luttrell Lab (Lee <i>et al.</i> , 2016)	N/A

1	CXCR3-SmBiT	This work	N/A
2	CXCR3- S355A/S356A -SmBiT	This work	N/A
3	CXCR3-T360A/S361A-/SmBiT	This work	N/A
4	CXCR3- T360A/S361A/S364A/S366A- SmBiT	This work	N/A
5	CXCR3-L344X-SmBiT	This work	N/A
6	GRK2-LgBiT	Asuka Inoue Lab	N/A
7	GRK3-LgBiT	Asuka Inoue Lab	N/A
8	GRK5-LgBiT	Asuka Inoue Lab	N/A
9	GRK6-LgBiT	Asuka Inoue Lab	N/A
10	pLenti-CXCR3	This work	N/A
11	pLenti-CXCR3-S355A/S356A	This work	N/A
12	pLenti-CXCR3-T360A/S361A	This work	N/A
13	pLenti-CXCR3- T360A/S361A/S364A/S366A	This work	N/A
14	pLenti-CXCR3- L344X	This work	N/A
15	pMD2.G	Addgene	Cat#12259; RRID:Addgene_12259
16	psPAX2	Addgene	Cat#12260; RRID:Addgene_12260
17	PX459	Addgene	Cat#62988; RRID:Addgene_62988
18	<b>Software and algorithms</b>		
19	GraphPad Prism	GraphPad Software	<a href="https://www.graphpad.com/scientific-software/prism/">https://www.graphpad.com/scientific-software/prism/</a>
20	ImageJ	(Schneider et al., 2012)	<a href="https://imagej.nih.gov/ij/">https://imagej.nih.gov/ij/</a>
21	Adobe Illustrator	Adobe	<a href="https://www.adobe.com/">https://www.adobe.com/</a>
22	Excel	Microsoft	<a href="https://www.microsoft.com/en-us/microsoft-365/excel">https://www.microsoft.com/en-us/microsoft-365/excel</a>
23	Database for Annotation, Visualization, and Integrated Discovery (DAVID)	(Huang da et al., 2009a; b)	<a href="https://david.ncifcrf.gov/home.jsp">https://david.ncifcrf.gov/home.jsp</a>
24	Kinase Enrichment Analysis	(Lachmann and Ma'ayan, 2009)	<a href="https://www.maayanlab.net/KEA2/">https://www.maayanlab.net/KEA2/</a>
25	Modification Motifs	(Bailey et al., 2006; Cheng et al., 2019)	<a href="https://meme-suite.org/meme/tools/momo">https://meme-suite.org/meme/tools/momo</a>
26	GProX	(Rigbolt et al., 2011)	<a href="http://qprox.sourceforge.net/">http://qprox.sourceforge.net/</a>
27	MaxQuant	(Tyanova et al., 2016a)	<a href="https://www.maxquant.org/">https://www.maxquant.org/</a>
28	FlowJo	Becton, Dickinson & Company	<a href="https://www.flowjo.com/">https://www.flowjo.com/</a>
29	ImageLab	Bio-Rad	<a href="https://www.bio-rad.com/en-us/product/image-lab-software">https://www.bio-rad.com/en-us/product/image-lab-software</a>
30	BioRender	BioRender	<a href="https://biorender.com/">https://biorender.com/</a>
31	GPCRdb	(Kooistra et al., 2021)	<a href="https://gpcrdb.org/">https://gpcrdb.org/</a>

1  
904 **SUPPLEMENTAL FIGURE TITLES AND LEGENDS**  
2  
905  
3  
906  
4

5  
907 **Supplemental Figure 1: Quantitation of CXCR3 C-terminal phosphopeptides and G protein activation, β-**  
6  
908 **arrestin-2 recruitment, and surface expression of various CXCR3 phosphodeficient mutants. Related to**  
7  
909 **Figure 1.**  
8

9  
909 Abundance of singly phosphorylated (A) RDpSSWSETSEASYSGL, (B) RDSpSWSETSEASYSGL, and (C)  
10 RDSSWSEpTSEASYSGL peptide following stimulation with vehicle control or 100 nM of chemokine for 5  
11 minutes. Mean ± SEM, n=2 technical replicates of 6 pooled biological replicates. P<.05, by one-way ANOVA,  
12 Tukey's post hoc analysis. (D-E) Agonist dose-dependent TGF-α shedding assay of CXCR3-WT and various  
13 phosphorylation deficient mutants to assess Gai1 and Gai3 protein activation. Mean ± SEM, n=3 (F-G) β-arrestin-  
14 2 recruitment of receptors treated with CXCL11. Mean ± SEM, n=3. (H) Surface expression of HEK293 cells  
15 transiently transfected with pcDNA 3.1 empty vector, CXCR3-WT, or denoted receptor as measured by flow  
16 cytometry. Mean ± SEM, n=3-5. \*P<.05 by one-way ANOVA, Dunnett's post hoc testing denotes comparisons  
17 to CXCR3-WT.  
18  
19

20 **Supplemental Figure 2: G protein dissociation in β-arrestin-1/2 knockout cells and phosphomimetic**  
21 **mutants, β-arrestin-2 recruitment grouped by receptor. Related to Figure 2.**  
22

23 (A-C) G protein dissociation of receptors treated with chemokine in β-arrestin-1/2 knockout cells. (D) G protein  
24 dissociation of CXCR3-S355A/S356A in β-arrestin-1/2 knockout cells. (E-G) G protein dissociation of CXCR3-  
25 WT, CXCR3-S355A/S356A, or phosphomimetic mutant CXCR3-S355D/S356D treated with chemokine. (H-L) β-  
26 arrestin-2 recruitment of receptors treated with chemokine as grouped by receptor. For (A-G) TRUPATH and (H-  
27 L) β-arrestin-2 recruitment assays, data shown are the mean ± SEM, n=3-4. \* denotes statistically significant  
28 differences between E<sub>Max</sub> of specified receptor and CXCR3-WT unless otherwise noted. Agonist dose-dependent  
29 data presented are the average of BRET values 5 to 10 minutes following ligand stimulation.  
30  
31

32 **Supplemental Figure 3: Single color confocal microscopy, and orthogonal BRET based receptor**  
33 **internalization assay. Related to Figure 2.**  
34  
35

1 (A-E) Confocal microscopy images of HEK293 cells transfected with Receptor-GFP and β-arrestin-2-RFP  
2 following treatment with vehicle control or 100 nM of the listed chemokine for 45 minutes. Images are  
3 representative of three biological replicates. (F) Schematic of BRET assay to detect receptor internalization away  
4 from the plasma membrane. (G) BRET data of receptor internalization using the acceptor Myrpalm-mVenus  
5 following stimulation with 100 nM of the listed chemokine in HEK293 cells. For internalization BRET (G) assays,  
6 data shown are the mean ± SEM, n=4. \*P<.05 by two-way ANOVA, Dunnett's post hoc testing between CXCR3-  
7 WT and all other receptor mutants at a specific ligand. Data presented are the average of BRET values from 20-  
8 30 minutes following ligand stimulation.  
9  
10  
11  
12  
13  
14  
15  
16  
17  
18  
19  
20  
21  
22

23 **Supplemental Figure 4: GRK5 and GRK6 Recruitment Data in wild-type HEK293 cells and GRK 2/3/5/6  
24 knockout cells. Related to Figure 3.**

25 Agonist dose-dependent data and kinetic data of maximum treatment dose of (A-C) GRK5 and (G-I) GRK6  
26 recruitment as measured by a split nanoluciferase assay in HEK293 cells. Data are grouped by ligand treatment.  
27  
28  
29  
30  
31 Agonist dose-dependent (D-F) GRK5 recruitment and (J-L) GRK6 recruitment as measured in GRK 2/3/5/6  
32  
33 knock out cells. Mean ± SEM, n=3.  
34  
35  
36  
37

38 **Supplemental Figure 5: GRK2 and GRK3 Recruitment Data as grouped by receptor and with  
39 phosphomimetic receptors. Related to Figure 3.**

40 Agonist dose-dependent data and kinetic data of maximum treatment dose of (A-E) GRK2 recruitment and (L-  
41  
42 P) GRK3 recruitment to listed receptor as measured by a split nanoluciferase assay. Data are grouped by  
43  
44 receptor. (F-K) GRK2 and (Q-V) GRK3 recruitment to phosphomimetic receptors (F-H, Q-S) CXCR3-  
45  
46 T360D/S361D, and (I-K, T-V) CXCR3-4xD. Mean ± SEM, n=3-4. \* denotes statistically significant differences  
47  
48 between E<sub>Max</sub> of specified receptor and CXCR3-WT. # denotes statistically significant differences between EC<sub>50</sub>  
49  
50 between E<sub>Max</sub> of specified receptor and CXCR3-WT. # denotes statistically significant differences between EC<sub>50</sub>  
51  
52 of specified receptor and CXCR3-WT.  
53  
54  
55  
56  
57

58 **Supplemental Figure 6: Source FIAsh Data. Related to Figure 3.**

59  
60  
61  
62  
63  
64  
65

1 (A-F) FlAsH data as grouped by FlAsH probes 1-6 shown as heat maps. Intensity of color corresponds with  
2 change in net BRET. (G) Source data for all FlAsH construct, ligand, receptor, combinations. Mean  $\pm$  SEM, n=5.  
3  
4 \*P<.05 by two-way ANOVA for each FlAsH construct are shown in the heat maps to demonstrate statistical  
5 significance of a ligand effect, receptor effect, and or interaction. If a significant interaction term was identified,  
6 Tukey's post hoc testing was performed, and comparisons are shown in panel (G).  
7  
8  
9  
10  
11  
12  
13  
14  
15

16 **Supplemental Figure 7: Structural model of the construct used in the molecular dynamics simulations.**

17  
18 **Related to Figure 4.** This model highlights the location of FlAsH probes 1-5 (red spheres) on  $\beta$ -arrestin 2 and  
19 the N-terminal RLuc (highlighted in green). We demonstrate the transition between an inactivate state with a low  
20 interdomain rotation angle, and an activate state, with a high interdomain rotation angle.  
21  
22  
23  
24  
25  
26

27 **Supplemental Figure 8: Approach and source data for mass spectrometry to assess the global**  
28  
29 **phosphoproteome. Related to Figure 5.**

30  
31 (A) Schematic of experimental design of global phosphoproteomics experiments. (B) Venn diagram showing  
32 number of proteins and phosphoproteins identified. (C) Source data describing the proteome and  
33 phosphoproteome where Class I phosphorylation sites are defined as those with a localization probability of at  
34 least 0.75 (Olsen et al., 2006). (D) TMT labelling intensity across samples and pooled data demonstrating high  
35 degrees of replicability. (E) Heatmap and dendrogram of individual pooled technical replicates of HEK293 cells  
36 treated with vehicle control, CXCL9, CXCL10, or CXCL11 demonstrating technical replicates of specific  
37 treatments cluster together. (F) Visual representation of GProX clustering.  
38  
39  
40  
41  
42  
43  
44  
45  
46  
47  
48

49 **Supplemental Figure 9: Quantification of ERK1/2 phosphorylation at 5 minutes as grouped by receptor.**

50  
51 **Related to Figure 6.**

52  
53 (A-E) Quantification of western blots of phosphorylated ERK1/2 in HEK293 cells expressing the indicated  
54 receptor following stimulation with vehicle control or 100 nM of chemokine at five minutes. Mean  $\pm$  SEM, n=4.  
55  
56  
57  
58 \*P<.05 by two-way ANOVA. Tukey's post hoc testing denotes comparisons between ligands. Chemokine  
59  
60 treatments were significantly different from vehicle at all receptors.  
61  
62  
63  
64  
65

1  
2  
3

4 **Supplemental Figure 10: Jurkat chemotaxis as grouped by receptor and univariate analyses of**  
5 **chemotaxis data. Related to Figure 7.**

6  
7  
8  
9 (A-F) Normalized Jurkat chemotaxis data grouped by CXCR3-KO or receptor. Mean  $\pm$  SEM, n=4. \*P<.05 by  
10  
11 two-way ANOVA, Tukey's post hoc testing. (G-I) Univariate linear regression of G Protein activation,  $\beta$ -arrestin  
12  
13 2 recruitment, and MAPK activation versus chemotaxis. Shown are the best fit lines and 95% confidence  
14  
15 intervals for each regression analysis. \*P<.05 by F-test to determine if the slope of the best fit line is non-zero.  
16

17  
18  
19  
20  
21  
22  
23  
24  
25  
26  
27  
28  
29  
30  
31  
32  
33  
34  
35  
36  
37  
38  
39  
40  
41  
42  
43  
44  
45  
46  
47  
48  
49  
50  
51  
52  
53  
54  
55  
56  
57  
58  
59  
60  
61  
62  
63  
64  
65

1  
2  
3  
4  
5  
6  
7  
8  
9  
10  
11  
12  
13  
14  
15  
16  
17  
18  
19  
20  
21  
22  
23  
24  
25  
26  
27  
28  
29  
30  
31  
32  
33  
34  
35  
36  
37  
38  
39  
40  
41  
42  
43  
44  
45  
46  
47  
48  
49  
50  
51  
52  
53  
54  
55  
56  
57  
58  
59  
60  
61  
62  
63  
64  
65  
REFERENCES

- 991 4 Allen, S.J., Crown, S.E., and Handel, T.M. (2007). Chemokine: receptor structure, interactions, and  
992 5 antagonism. *Annu Rev Immunol* 25, 787-820. 10.1146/annurev.immunol.24.021605.090529.  
993 6  
994 7 Alvarez-Curto, E., Inoue, A., Jenkins, L., Raihan, S.Z., Prihandoko, R., Tobin, A.B., and Milligan, G. (2016).  
995 8 Targeted Elimination of G Proteins and Arrestins Defines Their Specific Contributions to Both Intensity and  
996 9 Duration of G Protein-coupled Receptor Signaling. *J Biol Chem* 291, 27147-27159. 10.1074/jbc.M116.754887.  
997 10 Baidya, M., Kumari, P., Dwivedi-Agnihotri, H., Pandey, S., Chaturvedi, M., Stepniewski, T.M., Kawakami, K.,  
998 11 Cao, Y., Laporte, S.A., Selent, J., et al. (2020). Key phosphorylation sites in GPCRs orchestrate the  
999 12 contribution of beta-Arrestin 1 in ERK1/2 activation. *EMBO Rep* 21, e49886. 10.15252/embr.201949886.  
000 13 Bailey, T.L., Williams, N., Misleh, C., and Li, W.W. (2006). MEME: discovering and analyzing DNA and protein  
001 14 sequence motifs. *Nucleic Acids Res* 34, W369-373. 10.1093/nar/gkl198.  
002 15 Beausoleil, S.A., Villen, J., Gerber, S.A., Rush, J., and Gygi, S.P. (2006). A probability-based approach for  
003 17 high-throughput protein phosphorylation analysis and site localization. *Nat Biotechnol* 24, 1285-1292.  
004 18 10.1038/nbt1240.  
005 19 Bonacchi, A., Romagnani, P., Romanelli, R.G., Efsen, E., Annunziato, F., Lasagni, L., Francalanci, M., Serio,  
006 20 M., Laffi, G., Pinzani, M., et al. (2001). Signal transduction by the chemokine receptor CXCR3: activation of  
007 21 Ras/ERK, Src, and phosphatidylinositol 3-kinase/Akt controls cell migration and proliferation in human vascular  
008 22 pericytes. *J Biol Chem* 276, 9945-9954. 10.1074/jbc.M010303200.  
009 23 Bouzo-Lorenzo, M., Santo-Zas, I., Lodeiro, M., Nogueiras, R., Casanueva, F.F., Castro, M., Pazos, Y., Tobin,  
010 24 A.B., Butcher, A.J., and Camina, J.P. (2016). Distinct phosphorylation sites on the ghrelin receptor, GHSR1a,  
011 25 establish a code that determines the functions of ss-arrestins. *Sci Rep* 6, 22495. 10.1038/srep22495.  
012 27 Bradley, S.J., Molloy, C., Valuskaova, P., Dwomoh, L., Scarpa, M., Rossi, M., Finlayson, L., Svensson, K.A.,  
013 28 Chernet, E., Barth, V.N., et al. (2020). Biased M1-muscarinic-receptor-mutant mice inform the design of next-  
014 29 generation drugs. *Nat Chem Biol* 16, 240-249. 10.1038/s41589-019-0453-9.  
015 30 Busillo, J.M., Armando, S., Sengupta, R., Meucci, O., Bouvier, M., and Benovic, J.L. (2010). Site-specific  
016 31 phosphorylation of CXCR4 is dynamically regulated by multiple kinases and results in differential modulation of  
017 32 CXCR4 signaling. *J Biol Chem* 285, 7805-7817. 10.1074/jbc.M109.091173.  
018 33 Butcher, A.J., Prihandoko, R., Kong, K.C., McWilliams, P., Edwards, J.M., Bottrill, A., Mistry, S., and Tobin,  
019 34 A.B. (2011). Differential G-protein-coupled receptor phosphorylation provides evidence for a signaling bar  
020 36 code. *J Biol Chem* 286, 11506-11518. 10.1074/jbc.M110.154526.  
021 37 Cahill, T.J., 3rd, Thomsen, A.R., Tarrasch, J.T., Plouffe, B., Nguyen, A.H., Yang, F., Huang, L.Y., Kahsai,  
022 38 A.W., Bassoni, D.L., Gavino, B.J., et al. (2017). Distinct conformations of GPCR-beta-arrestin complexes  
023 39 mediate desensitization, signaling, and endocytosis. *Proc Natl Acad Sci U S A* 114, 2562-2567.  
024 40 10.1073/pnas.1701529114.  
025 41 Chen, Q., Perry, N.A., Vishnivetskiy, S.A., Berndt, S., Gilbert, N.C., Zhuo, Y., Singh, P.K., Tholen, J., Ohi,  
026 42 M.D., Gurevich, E.V., et al. (2017). Structural basis of arrestin-3 activation and signaling. *Nat Commun* 8, 1427.  
027 43 10.1038/s41467-017-01218-8.  
028 44 Cheng, A., Grant, C.E., Noble, W.S., and Bailey, T.L. (2019). MoMo: discovery of statistically significant post-  
029 46 translational modification motifs. *Bioinformatics* 35, 2774-2782. 10.1093/bioinformatics/bty1058.  
030 47 Chow, M.T., Ozga, A.J., Servis, R.L., Frederick, D.T., Lo, J.A., Fisher, D.E., Freeman, G.J., Boland, G.M., and  
031 48 Luster, A.D. (2019). Intratumoral Activity of the CXCR3 Chemokine System Is Required for the Efficacy of Anti-  
032 49 PD-1 Therapy. *Immunity* 50, 1498-1512 e1495. 10.1016/j.jimmuni.2019.04.010.  
033 50 Colvin, R.A., Campanella, G.S., Manice, L.A., and Luster, A.D. (2006). CXCR3 requires tyrosine sulfation for  
034 51 ligand binding and a second extracellular loop arginine residue for ligand-induced chemotaxis. *Mol Cell Biol* 26,  
035 52 5838-5849. 10.1128/MCB.00556-06.  
036 53 Colvin, R.A., Campanella, G.S., Sun, J., and Luster, A.D. (2004). Intracellular domains of CXCR3 that mediate  
037 55 CXCL9, CXCL10, and CXCL11 function. *J Biol Chem* 279, 30219-30227. 10.1074/jbc.M403595200.  
038 56 Corbisier, J., Gales, C., Huszagh, A., Parmentier, M., and Springael, J.Y. (2015). Biased signaling at  
039 57 chemokine receptors. *J Biol Chem* 290, 9542-9554. 10.1074/jbc.M114.596098.  
040 58 Cox, J., and Mann, M. (2008). MaxQuant enables high peptide identification rates, individualized p.p.b.-range  
041 59 mass accuracies and proteome-wide protein quantification. *Nat Biotechnol* 26, 1367-1372. 10.1038/nbt.1511.  
042 60 Dwivedi-Agnihotri, H., Chaturvedi, M., Baidya, M., Stepniewski, T.M., Pandey, S., Maharana, J., Srivastava, A.,  
043 61 Caengprasath, N., Hanyaloglu, A.C., Selent, J., and Shukla, A.K. (2020). Distinct phosphorylation sites in a  
044 62  
045 63  
046 64  
047 65

- 1 prototypical GPCR differently orchestrate beta-arrestin interaction, trafficking, and signaling. *Sci Adv* 6.  
2 10.1126/sciadv.abb8368.  
3  
4 Eichel, K., Jullie, D., Barsi-Rhyne, B., Latorraca, N.R., Masureel, M., Sibarita, J.B., Dror, R.O., and von  
5 Zastrow, M. (2018). Catalytic activation of beta-arrestin by GPCRs. *Nature* 557, 381-386. 10.1038/s41586-018-  
6 0079-1.  
7  
8 Eiger, D.S., Boldizsar, N., Honeycutt, C.C., Gardner, J., and Rajagopal, S. (2021). Biased agonism at  
9 chemokine receptors. *Cell Signal* 78, 109862. 10.1016/j.cellsig.2020.109862.  
10 Ferguson, S.S., Downey, W.E., 3rd, Colapietro, A.M., Barak, L.S., Menard, L., and Caron, M.G. (1996). Role of  
11 beta-arrestin in mediating agonist-promoted G protein-coupled receptor internalization. *Science* 271, 363-366.  
12 10.1126/science.271.5247.363.  
13 Ge, L., Ly, Y., Hollenberg, M., and DeFea, K. (2003). A beta-arrestin-dependent scaffold is associated with  
14 prolonged MAPK activation in pseudopodia during protease-activated receptor-2-induced chemotaxis. *J Biol  
15 Chem* 278, 34418-34426. 10.1074/jbc.M300573200.  
16 Griffith, J.W., Sokol, C.L., and Luster, A.D. (2014). Chemokines and chemokine receptors: positioning cells for  
17 host defense and immunity. *Annu Rev Immunol* 32, 659-702. 10.1146/annurev-immunol-032713-120145.  
18 Gurevich, V.V., and Gurevich, E.V. (2004). The molecular acrobatics of arrestin activation. *Trends Pharmacol  
19 Sci* 25, 105-111. 10.1016/j.tips.2003.12.008.  
20 Gurevich, V.V., and Gurevich, E.V. (2019). GPCR Signaling Regulation: The Role of GRKs and Arrestins.  
21 *Front Pharmacol* 10, 125. 10.3389/fphar.2019.00125.  
22 Harvey, M.J., Giupponi, G., and Fabritiis, G.D. (2009). ACEMD: Accelerating Biomolecular Dynamics in the  
23 Microsecond Time Scale. *J Chem Theory Comput* 5, 1632-1639. 10.1021/ct9000685.  
24 Hauser, A.S., Attwood, M.M., Rask-Andersen, M., Schioth, H.B., and Gloriam, D.E. (2017). Trends in GPCR  
25 drug discovery: new agents, targets and indications. *Nat Rev Drug Discov* 16, 829-842. 10.1038/nrd.2017.178.  
26 He, Q.T., Xiao, P., Huang, S.M., Jia, Y.L., Zhu, Z.L., Lin, J.Y., Yang, F., Tao, X.N., Zhao, R.J., Gao, F.Y., et al.  
27 (2021). Structural studies of phosphorylation-dependent interactions between the V2R receptor and arrestin-2.  
28 *Nat Commun* 12, 2396. 10.1038/s41467-021-22731-x.  
29 Huang da, W., Sherman, B.T., and Lempicki, R.A. (2009a). Bioinformatics enrichment tools: paths toward the  
30 comprehensive functional analysis of large gene lists. *Nucleic Acids Res* 37, 1-13. 10.1093/nar/gkn923.  
31 Huang da, W., Sherman, B.T., and Lempicki, R.A. (2009b). Systematic and integrative analysis of large gene  
32 lists using DAVID bioinformatics resources. *Nat Protoc* 4, 44-57. 10.1038/nprot.2008.211.  
33 Huang, J., Rauscher, S., Nawrocki, G., Ran, T., Feig, M., de Groot, B.L., Grubmuller, H., and MacKerell, A.D.,  
34 Jr. (2017). CHARMM36m: an improved force field for folded and intrinsically disordered proteins. *Nat Methods*  
35 14, 71-73. 10.1038/nmeth.4067.  
36 Inagaki, S., Ghirlando, R., Vishnivetskiy, S.A., Homan, K.T., White, J.F., Tesmer, J.J., Gurevich, V.V., and  
37 Grisshammer, R. (2015). G Protein-Coupled Receptor Kinase 2 (GRK2) and 5 (GRK5) Exhibit Selective  
38 Phosphorylation of the Neurotensin Receptor in Vitro. *Biochemistry* 54, 4320-4329.  
39 10.1021/acs.biochem.5b00285.  
40 Inoue, A., Ishiguro, J., Kitamura, H., Arima, N., Okutani, M., Shuto, A., Higashiyama, S., Ohwada, T., Arai, H.,  
41 Makide, K., and Aoki, J. (2012). TGFalpha shedding assay: an accurate and versatile method for detecting  
42 GPCR activation. *Nat Methods* 9, 1021-1029. 10.1038/nmeth.2172.  
43 Inoue, A., Raimondi, F., Kadji, F.M.N., Singh, G., Kishi, T., Uwamizu, A., Ono, Y., Shinjo, Y., Ishida, S., Arang,  
44 N., et al. (2019). Illuminating G-Protein-Coupling Selectivity of GPCRs. *Cell* 177, 1933-1947 e1925.  
45 10.1016/j.cell.2019.04.044.  
46 Jung, S.R., Kushmerick, C., Seo, J.B., Koh, D.S., and Hille, B. (2017). Muscarinic receptor regulates  
47 extracellular signal regulated kinase by two modes of arrestin binding. *Proc Natl Acad Sci U S A* 114, E5579-  
48 E5588. 10.1073/pnas.1700331114.  
49 Kahsai, A.W., Pani, B., and Lefkowitz, R.J. (2018). GPCR signaling: conformational activation of arrestins. *Cell  
50 Res* 28, 783-784. 10.1038/s41422-018-0067-x.  
51 Kaya, A.I., Perry, N.A., Gurevich, V.V., and Iverson, T.M. (2020). Phosphorylation barcode-dependent signal  
52 bias of the dopamine D1 receptor. *Proc Natl Acad Sci U S A* 117, 14139-14149. 10.1073/pnas.1918736117.  
53 Keshava Prasad, T.S., Goel, R., Kandasamy, K., Keerthikumar, S., Kumar, S., Mathivanan, S., Telikicherla, D.,  
54 Raju, R., Shafreen, B., Venugopal, A., et al. (2009). Human Protein Reference Database--2009 update.  
55 *Nucleic Acids Res* 37, D767-772. 10.1093/nar/gkn892.  
56  
57  
58  
59  
60  
61  
62  
63  
64  
65

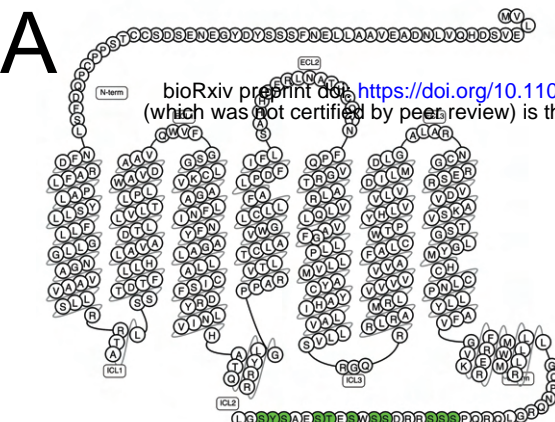
- 1  
2 Kim, Y.M., and Benovic, J.L. (2002). Differential roles of arrestin-2 interaction with clathrin and adaptor protein  
3 2 in G protein-coupled receptor trafficking. *J Biol Chem* 277, 30760-30768. 10.1074/jbc.M204528200.  
4  
5 Kliewer, A., Schmiedel, F., Sianati, S., Bailey, A., Bateman, J.T., Levitt, E.S., Williams, J.T., Christie, M.J., and  
6 Schulz, S. (2019). Phosphorylation-deficient G-protein-biased mu-opioid receptors improve analgesia and  
7 diminish tolerance but worsen opioid side effects. *Nat Commun* 10, 367. 10.1038/s41467-018-08162-1.  
8 Komolov, K.E., and Benovic, J.L. (2018). G protein-coupled receptor kinases: Past, present and future. *Cell  
9 Signal* 41, 17-24. 10.1016/j.cellsig.2017.07.004.  
10 Kooistra, A.J., Mordalski, S., Pandy-Szekeres, G., Esguerra, M., Mamyrbekov, A., Munk, C., Keseru, G.M., and  
11 Gloriam, D.E. (2021). GPCRdb in 2021: integrating GPCR sequence, structure and function. *Nucleic Acids Res  
12* 49, D335-D343. 10.1093/nar/gkaa1080.  
13 Kufareva, I., Salanga, C.L., and Handel, T.M. (2015). Chemokine and chemokine receptor structure and  
14 interactions: implications for therapeutic strategies. *Immunol Cell Biol* 93, 372-383. 10.1038/icb.2015.15.  
15 Kuo, P.T., Zeng, Z., Salim, N., Mattarollo, S., Wells, J.W., and Leggatt, G.R. (2018). The Role of CXCR3 and  
16 Its Chemokine Ligands in Skin Disease and Cancer. *Front Med (Lausanne)* 5, 271. 10.3389/fmed.2018.00271.  
17 Lachmann, A., and Ma'ayan, A. (2009). KEA: kinase enrichment analysis. *Bioinformatics* 25, 684-686.  
18 10.1093/bioinformatics/btp026.  
19 Laporte, S.A., Oakley, R.H., Zhang, J., Holt, J.A., Ferguson, S.S., Caron, M.G., and Barak, L.S. (1999). The  
20 beta2-adrenergic receptor/betaarrestin complex recruits the clathrin adaptor AP-2 during endocytosis. *Proc  
21 Natl Acad Sci U S A* 96, 3712-3717. 10.1073/pnas.96.7.3712.  
22 Latorraca, N.R., Masureel, M., Hollingsworth, S.A., Heydenreich, F.M., Suomivuori, C.M., Brinton, C.,  
23 Townshend, R.J.L., Bouvier, M., Kobilka, B.K., and Dror, R.O. (2020). How GPCR Phosphorylation Patterns  
24 Orchestrate Arrestin-Mediated Signaling. *Cell* 183, 1813-1825 e1818. 10.1016/j.cell.2020.11.014.  
25 Latorraca, N.R., Wang, J.K., Bauer, B., Townshend, R.J.L., Hollingsworth, S.A., Olivieri, J.E., Xu, H.E.,  
26 Sommer, M.E., and Dror, R.O. (2018). Molecular mechanism of GPCR-mediated arrestin activation. *Nature  
27* 557, 452-456. 10.1038/s41586-018-0077-3.  
28 Lee, M.H., Appleton, K.M., Strungs, E.G., Kwon, J.Y., Morinelli, T.A., Peterson, Y.K., Laporte, S.A., and  
29 Luttrell, L.M. (2016). The conformational signature of beta-arrestin2 predicts its trafficking and signalling  
30 functions. *Nature* 531, 665-668. 10.1038/nature17154.  
31 Lin, R., Choi, Y.H., Zidar, D.A., and Walker, J.K.L. (2018). beta-Arrestin-2-Dependent Signaling Promotes  
32 CCR4-mediated Chemotaxis of Murine T-Helper Type 2 Cells. *Am J Respir Cell Mol Biol* 58, 745-755.  
33 10.1165/rcmb.2017-0240OC.  
34 Luttrell, L.M., Wang, J., Plouffe, B., Smith, J.S., Yamani, L., Kaur, S., Jean-Charles, P.Y., Gauthier, C., Lee,  
35 M.H., Pani, B., et al. (2018). Manifold roles of beta-arrestins in GPCR signaling elucidated with siRNA and  
36 CRISPR/Cas9. *Sci Signal* 11. 10.1126/scisignal.aat7650.  
37 Mann, A., Liebetrau, S., Klima, M., Dasgupta, P., Massotte, D., and Schulz, S. (2020). Agonist-induced  
38 phosphorylation bar code and differential post-activation signaling of the delta opioid receptor revealed by  
39 phosphosite-specific antibodies. *Sci Rep* 10, 8585. 10.1038/s41598-020-65589-7.  
40 Mantovani, A. (1999). The chemokine system: redundancy for robust outputs. *Immunol Today* 20, 254-257.  
41 10.1016/s0167-5699(99)01469-3.  
42 Marsango, S., Ward, R.J., Jenkins, L., Butcher, A.J., Al Mahmud, Z., Dwomoh, L., Nagel, F., Schulz, S.,  
43 Tikhonova, I.G., Tobin, A.B., and Milligan, G. (2022). Selective phosphorylation of threonine residues defines  
44 GPR84-arrestin interactions of biased ligands. *J Biol Chem* 298, 101932. 10.1016/j.jbc.2022.101932.  
45 Mayer, D., Damberger, F.F., Samarasimhareddy, M., Feldmueller, M., Vuckovic, Z., Flock, T., Bauer, B., Mutt,  
46 E., Zosel, F., Allain, F.H.T., et al. (2019). Distinct G protein-coupled receptor phosphorylation motifs modulate  
47 arrestin affinity and activation and global conformation. *Nat Commun* 10, 1261. 10.1038/s41467-019-09204-y.  
48 Mertins, P., Tang, L.C., Krug, K., Clark, D.J., Gritsenko, M.A., Chen, L., Clauser, K.R., Clauss, T.R., Shah, P.,  
49 Gillette, M.A., et al. (2018). Reproducible workflow for multiplexed deep-scale proteome and phosphoproteome  
50 analysis of tumor tissues by liquid chromatography-mass spectrometry. *Nat Protoc* 13, 1632-1661.  
51 10.1038/s41596-018-0006-9.  
52 Miess, E., Gondin, A.B., Yousuf, A., Steinborn, R., Mosslein, N., Yang, Y., Goldner, M., Ruland, J.G.,  
53 Bunemann, M., Krasel, C., et al. (2018). Multisite phosphorylation is required for sustained interaction with  
54 GRKs and arrestins during rapid mu-opioid receptor desensitization. *Sci Signal* 11. 10.1126/scisignal.aas9609.  
55  
56  
57  
58  
59  
60  
61  
62  
63  
64  
65

- 1  
149 2 Nobles, K.N., Xiao, K., Ahn, S., Shukla, A.K., Lam, C.M., Rajagopal, S., Strachan, R.T., Huang, T.Y., Bressler,  
150 3 E.A., Hara, M.R., et al. (2011). Distinct phosphorylation sites on the beta(2)-adrenergic receptor establish a  
151 4 barcode that encodes differential functions of beta-arrestin. *Sci Signal* 4, ra51. 10.1126/scisignal.2001707.  
152 5 Nuber, S., Zabel, U., Lorenz, K., Nuber, A., Milligan, G., Tobin, A.B., Lohse, M.J., and Hoffmann, C. (2016).  
153 6 beta-Arrestin biosensors reveal a rapid, receptor-dependent activation/deactivation cycle. *Nature* 531, 661-  
154 7 664. 10.1038/nature17198.  
155 8 Oakley, R.H., Laporte, S.A., Holt, J.A., Barak, L.S., and Caron, M.G. (1999). Association of beta-arrestin with G  
156 9 protein-coupled receptors during clathrin-mediated endocytosis dictates the profile of receptor resensitization. *J  
157 10 Biol Chem* 274, 32248-32257. 10.1074/jbc.274.45.32248.  
158 11 Olsen, J.V., Blagoev, B., Ghad, F., Macek, B., Kumar, C., Mortensen, P., and Mann, M. (2006). Global, in vivo,  
159 12 and site-specific phosphorylation dynamics in signaling networks. *Cell* 127, 635-648.  
160 13 10.1016/j.cell.2006.09.026.  
161 14 Olsen, R.H.J., DiBerto, J.F., English, J.G., Glaudin, A.M., Krumm, B.E., Slocum, S.T., Che, T., Gavin, A.C.,  
162 15 McCory, J.D., Roth, B.L., and Strachan, R.T. (2020). TRUPATH, an open-source biosensor platform for  
163 16 interrogating the GPCR transducerome. *Nat Chem Biol* 16, 841-849. 10.1038/s41589-020-0535-8.  
164 17 Pack, T.F., Orlen, M.I., Ray, C., Peterson, S.M., and Caron, M.G. (2018). The dopamine D2 receptor can  
165 18 directly recruit and activate GRK2 without G protein activation. *J Biol Chem* 293, 6161-6171.  
166 19 10.1074/jbc.RA117.001300.  
167 20 Pandey, S., Kumari, P., Baidya, M., Kise, R., Cao, Y., Dwivedi-Agnihotri, H., Banerjee, R., Li, X.X., Cui, C.S.,  
168 21 Lee, J.D., et al. (2021a). Intrinsic bias at non-canonical, beta-arrestin-coupled seven transmembrane  
169 22 receptors. *Mol Cell* 81, 4605-4621 e4611. 10.1016/j.molcel.2021.09.007.  
170 23 Pandey, S., Kumari, P., Baidya, M., Kise, R., Cao, Y., Dwivedi-Agnihotri, H., Banerjee, R., Li, X.X., Cui, C.S.,  
171 24 Lee, J.D., et al. (2021b). Intrinsic bias at non-canonical, beta-arrestin-coupled seven transmembrane  
172 25 receptors. *Mol Cell*. 10.1016/j.molcel.2021.09.007.  
173 26 Pupo, A.S., Duarte, D.A., Lima, V., Teixeira, L.B., Parreira, E.S.L.T., and Costa-Neto, C.M. (2016). Recent  
174 27 updates on GPCR biased agonism. *Pharmacol Res* 112, 49-57. 10.1016/j.phrs.2016.01.031.  
175 28 Rajagopal, S., Bassoni, D.L., Campbell, J.J., Gerard, N.P., Gerard, C., and Wehrman, T.S. (2013). Biased  
176 29 agonism as a mechanism for differential signaling by chemokine receptors. *The Journal of biological chemistry*  
177 30 288, 35039-35048. 10.1074/jbc.M113.479113.  
178 31 Ribas, C., Penela, P., Murga, C., Salcedo, A., Garcia-Hoz, C., Jurado-Pueyo, M., Aymerich, I., and Mayor, F.,  
179 32 Jr. (2007). The G protein-coupled receptor kinase (GRK) interactome: role of GRKs in GPCR regulation and  
180 33 signaling. *Biochim Biophys Acta* 1768, 913-922. 10.1016/j.bbamem.2006.09.019.  
181 34 Rigbolt, K.T., Vanselow, J.T., and Blagoev, B. (2011). GProX, a user-friendly platform for bioinformatics  
182 35 analysis and visualization of quantitative proteomics data. *Mol Cell Proteomics* 10, O110 007450.  
183 36 10.1074/mcp.O110.007450.  
184 37 Rodriguez-Espigares, I., Torrens-Fontanals, M., Tiemann, J.K.S., Aranda-Garcia, D., Ramirez-Anguita, J.M.,  
185 38 Stepniewski, T.M., Worp, N., Varela-Rial, A., Morales-Pastor, A., Medel-Lacruz, B., et al. (2020). GPCRmd  
186 39 uncovers the dynamics of the 3D-GPCRome. *Nat Methods* 17, 777-787. 10.1038/s41592-020-0884-y.  
187 40 Sato, P.Y., Chuprun, J.K., Schwartz, M., and Koch, W.J. (2015). The evolving impact of g protein-coupled  
188 41 receptor kinases in cardiac health and disease. *Physiol Rev* 95, 377-404. 10.1152/physrev.00015.2014.  
189 42 Scarpa, M., Molloy, C., Jenkins, L., Strellis, B., Budgett, R.F., Hesse, S., Dwomoh, L., Marsango, S., Tejeda,  
190 43 G.S., Rossi, M., et al. (2021). Biased M1 muscarinic receptor mutant mice show accelerated progression of  
191 44 prion neurodegenerative disease. *Proc Natl Acad Sci U S A* 118. 10.1073/pnas.2107389118.  
192 45 Schneider, C.A., Rasband, W.S., and Eliceiri, K.W. (2012). NIH Image to ImageJ: 25 years of image analysis.  
193 46 *Nat Methods* 9, 671-675. 10.1038/nmeth.2089.  
194 47 Sente, A., Peer, R., Srivastava, A., Baidya, M., Lesk, A.M., Balaji, S., Shukla, A.K., Babu, M.M., and Flock, T.  
195 48 (2018). Molecular mechanism of modulating arrestin conformation by GPCR phosphorylation. *Nat Struct Mol  
196 49 Biol* 25, 538-545. 10.1038/s41594-018-0071-3.  
197 50 Shahabuddin, S., Ji, R., Wang, P., Brailoiu, E., Dun, N., Yang, Y., Aksoy, M.O., and Kelsen, S.G. (2006).  
198 51 CXCR3 chemokine receptor-induced chemotaxis in human airway epithelial cells: role of p38 MAPK and PI3K  
199 52 signaling pathways. *Am J Physiol Cell Physiol* 291, C34-39. 10.1152/ajpcell.00441.2005.  
200 53 Shi, Y., Kornovski, B.S., Savani, R., and Turley, E.A. (1993). A rapid, multiwell colorimetric assay for  
201 54 chemotaxis. *J Immunol Methods* 164, 149-154. 10.1016/0022-1759(93)90307-s.  
61  
62  
63  
64  
65

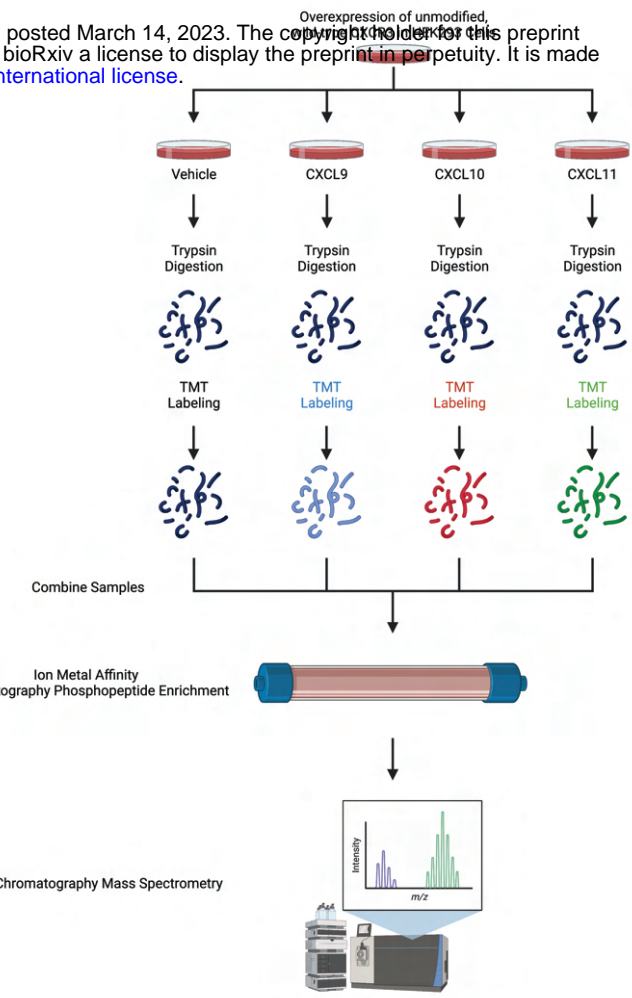
- 1  
2 Shukla, A.K., Manglik, A., Kruse, A.C., Xiao, K., Reis, R.I., Tseng, W.C., Staus, D.P., Hilger, D., Uysal, S.,  
3 Huang, L.Y., et al. (2013). Structure of active beta-arrestin-1 bound to a G-protein-coupled receptor  
4 phosphopeptide. *Nature* 497, 137-141. 10.1038/nature12120.  
5 Shukla, A.K., Violin, J.D., Whalen, E.J., Gesty-Palmer, D., Shenoy, S.K., and Lefkowitz, R.J. (2008). Distinct  
6 conformational changes in beta-arrestin report biased agonism at seven-transmembrane receptors. *Proc Natl  
7 Acad Sci U S A* 105, 9988-9993. 10.1073/pnas.0804246105.  
8 Smith, J.S., Alagesan, P., Desai, N.K., Pack, T.F., Wu, J.H., Inoue, A., Freedman, N.J., and Rajagopal, S.  
9 (2017). C-X-C Motif Chemokine Receptor 3 Splice Variants Differentially Activate Beta-Arrestins to Regulate  
10 Downstream Signaling Pathways. *Molecular pharmacology* 92, 136-150. 10.1124/mol.117.108522.  
11 Smith, J.S., Nicholson, L.T., Suwanpradid, J., Glenn, R.A., Knape, N.M., Alagesan, P., Gundry, J.N.,  
12 Wehrman, T.S., Atwater, A.R., Gunn, M.D., et al. (2018a). Biased agonists of the chemokine receptor CXCR3  
13 differentially control chemotaxis and inflammation. *Science Signaling* 11, eaaq1075.  
14 10.1126/scisignal.aaq1075.  
15 Smith, J.S., Nicholson, L.T., Suwanpradid, J., Glenn, R.A., Knape, N.M., Alagesan, P., Gundry, J.N.,  
16 Wehrman, T.S., Atwater, A.R., Gunn, M.D., et al. (2018b). Biased agonists of the chemokine receptor CXCR3  
17 differentially control chemotaxis and inflammation. *Sci Signal* 11. 10.1126/scisignal.aaq1075.  
18 Smith, J.S., Pack, T.F., Inoue, A., Lee, C., Zheng, K., Choi, I., Eiger, D.S., Warman, A., Xiong, X., Ma, Z., et al.  
19 (2021). Noncanonical scaffolding of Galphai and beta-arrestin by G protein-coupled receptors. *Science* 371.  
20 10.1126/science.ayy1833.  
21 Smith, J.S., and Rajagopal, S. (2016). The beta-Arrestins: Multifunctional Regulators of G Protein-coupled  
22 Receptors. *J Biol Chem* 291, 8969-8977. 10.1074/jbc.R115.713313.  
23 Smith, J.S., Rajagopal, S., and Atwater, A.R. (2018c). Chemokine Signaling in Allergic Contact Dermatitis:  
24 Toward Targeted Therapies. *Dermatitis* 29, 179-186. 10.1097/DER.0000000000000391.  
25 Stevers, L.M., Sijbesma, E., Botta, M., MacKintosh, C., Obsil, T., Landrieu, I., Cau, Y., Wilson, A.J.,  
26 Karawajczyk, A., Eickhoff, J., et al. (2018). Modulators of 14-3-3 Protein-Protein Interactions. *J Med Chem* 61,  
27 3755-3778. 10.1021/acs.jmedchem.7b00574.  
28 Strungs, E.G., Luttrell, L.M., and Lee, M.H. (2019). Probing Arrestin Function Using Intramolecular FIAsh-  
29 BRET Biosensors. *Methods Mol Biol* 1957, 309-322. 10.1007/978-1-4939-9158-7\_19.  
30 Sun, Y., Cheng, Z., Ma, L., and Pei, G. (2002). Beta-arrestin2 is critically involved in CXCR4-mediated  
31 chemotaxis, and this is mediated by its enhancement of p38 MAPK activation. *J Biol Chem* 277, 49212-49219.  
32 10.1074/jbc.M207294200.  
33 Tobin, A.B. (2008). G-protein-coupled receptor phosphorylation: where, when and by whom. *Br J Pharmacol*  
34 153 Suppl 1, S167-176. 10.1038/sj.bjp.0707662.  
35 Tsai, C.F., Smith, J.S., Krajewski, K., Zhao, R., Moghieb, A.M., Nicora, C.D., Xiong, X., Moore, R.J., Liu, T.,  
36 Smith, R.D., et al. (2019). Tandem Mass Tag Labeling Facilitates Reversed-Phase Liquid Chromatography-  
37 Mass Spectrometry Analysis of Hydrophilic Phosphopeptides. *Anal Chem* 91, 11606-11613.  
38 10.1021/acs.analchem.9b01814.  
39 Tsai, C.F., Zhao, R., Williams, S.M., Moore, R.J., Schultz, K., Chrisler, W.B., Pasa-Tolic, L., Rodland, K.D.,  
40 Smith, R.D., Shi, T., et al. (2020). An Improved Boosting to Amplify Signal with Isobaric Labeling (iBASIL)  
41 Strategy for Precise Quantitative Single-cell Proteomics. *Mol Cell Proteomics* 19, 828-838.  
42 10.1074/mcp.RA119.001857.  
43 Tyanova, S., Temu, T., and Cox, J. (2016a). The MaxQuant computational platform for mass spectrometry-  
44 based shotgun proteomics. *Nat Protoc* 11, 2301-2319. 10.1038/nprot.2016.136.  
45 Tyanova, S., Temu, T., Sinitcyn, P., Carlson, A., Hein, M.Y., Geiger, T., Mann, M., and Cox, J. (2016b). The  
46 Perseus computational platform for comprehensive analysis of (prote)omics data. *Nat Methods* 13, 731-740.  
47 10.1038/nmeth.3901.  
48 Watanabe, N., and Osada, H. (2012). Phosphorylation-dependent protein-protein interaction modules as  
49 potential molecular targets for cancer therapy. *Curr Drug Targets* 13, 1654-1658.  
50 10.2174/138945012803530035.  
51 Watanabe, Y., Yoshizawa, A.C., Ishihama, Y., and Okuda, S. (2021). The jPOST Repository as a Public Data  
52 Repository for Shotgun Proteomics. *Methods Mol Biol* 2259, 309-322. 10.1007/978-1-0716-1178-4\_20.  
53 Xiao, K., Shenoy, S.K., Nobles, K., and Lefkowitz, R.J. (2004). Activation-dependent conformational changes  
54 in {beta}-arrestin 2. *J Biol Chem* 279, 55744-55753. 10.1074/jbc.M409785200.  
55  
56  
57  
58  
59  
60  
61  
62  
63  
64  
65

- 1  
2 Yang, F., Yu, X., Liu, C., Qu, C.X., Gong, Z., Liu, H.D., Li, F.H., Wang, H.M., He, D.F., Yi, F., et al. (2015).  
3 Phospho-selective mechanisms of arrestin conformations and functions revealed by unnatural amino acid  
4 incorporation and (19)F-NMR. *Nat Commun* 6, 8202. 10.1038/ncomms9202.  
5 Yang, Z., Yang, F., Zhang, D., Liu, Z., Lin, A., Liu, C., Xiao, P., Yu, X., and Sun, J.P. (2017). Phosphorylation  
6 of G Protein-Coupled Receptors: From the Barcode Hypothesis to the Flute Model. *Mol Pharmacol* 92, 201-  
7 210. 10.1124/mol.116.107839.  
8 Zheng, K., Smith, J.S., Eiger, D.S., Warman, A., Choi, I., Honeycutt, C.C., Boldizsar, N., Gundry, J.N., Pack,  
9 T.F., Inoue, A., et al. (2022). Biased agonists of the chemokine receptor CXCR3 differentially signal through  
10 Galphai:beta-arrestin complexes. *Sci Signal* 15, eabg5203. 10.1126/scisignal.abg5203.  
11 Zhou, X.E., He, Y., de Waal, P.W., Gao, X., Kang, Y., Van Eps, N., Yin, Y., Pal, K., Goswami, D., White, T.A.,  
12 et al. (2017). Identification of Phosphorylation Codes for Arrestin Recruitment by G Protein-Coupled Receptors.  
13 *Cell* 170, 457-469 e413. 10.1016/j.cell.2017.07.002.  
14 Zlotnik, A., and Yoshie, O. (2012). The chemokine superfamily revisited. *Immunity* 36, 705-716.  
15 10.1016/j.jimmuni.2012.05.008.  
16  
17  
18  
19  
20  
21  
22  
23  
24  
25  
26  
27  
28  
29  
30  
31  
32  
33  
34  
35  
36  
37  
38  
39  
40  
41  
42  
43  
44  
45  
46  
47  
48  
49  
50  
51  
52  
53  
54  
55  
56  
57  
58  
59  
60  
61  
62  
63  
64  
65

# FIGURE 1



**B**

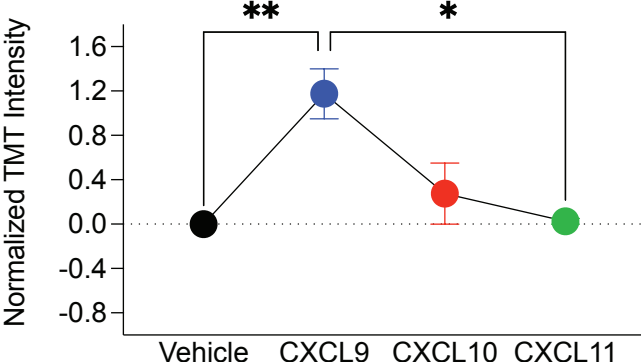


**C**

Number of Phosphorylation Sites	Modified Peptide Sequence	S355	S356	S358	T360	S361	S364	Y365	S366
One	DS <sup>Y</sup> WSETSEASYSGL								
	DSS <sup>Y</sup> WSETSEASYSGL								
	DSSWSET <sup>S</sup> EASYSGL								
	DSSWS <sup>T</sup> ETSEASYSGL								
	DSSWSET <sup>T</sup> SEASYSGL								
	DSSWSETSEAS <sup>Y</sup> SGL								
	DSSWSETSEASY <sup>S</sup> GL								
	RDSSWSETSEA <sup>S</sup> YSGL								
	RDSSWSET <sup>S</sup> EASYSGL								
	RDS <sup>S</sup> WSETSEASYSGL								
	RDS <sup>S</sup> WSETSEASYSGL								
	RDSSWSET <sup>T</sup> SEASYSGL								
Two	RDSSWSET <sup>S</sup> ETSEAS <sup>Y</sup> SGL								
	RDS <sup>S</sup> S <sup>T</sup> WSETSEASYSGL								
Three	RDS <sup>S</sup> WSET <sup>T</sup> <sup>S</sup> EASYSGL								
	RDS <sup>S</sup> WSET <sup>S</sup> <sup>T</sup> EASYSGL								
	RDS <sup>S</sup> WSET <sup>S</sup> <sup>T</sup> <sup>S</sup> EASYSGL								

**D**

DSSWSETSEASY<sup>S</sup>GL (S366)



**E**

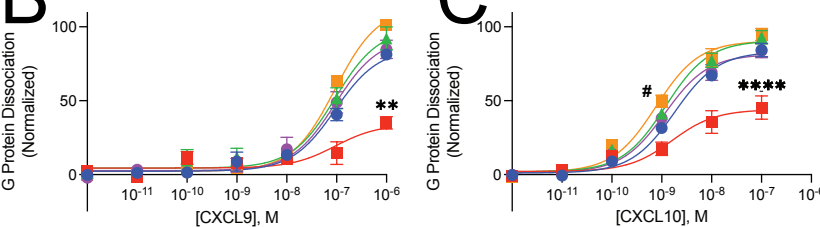


# FIGURE 2

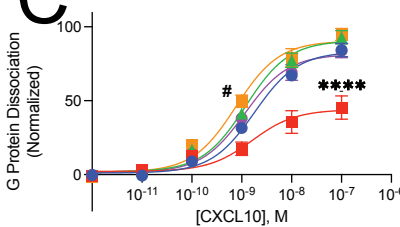
## G Protein Dissociation

bioRxiv preprint doi: <https://doi.org/10.1101/2023.03.14.532634>; this version posted March 14, 2023. The copyright holder for this preprint (which was not certified by peer review) is the author/funder, who has granted bioRxiv a license to display the preprint in perpetuity. It is made available under aCC-BY-NC 4.0 International license.

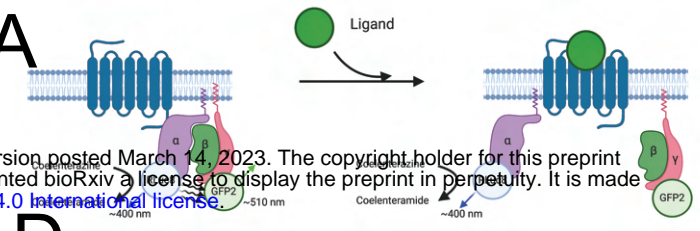
B



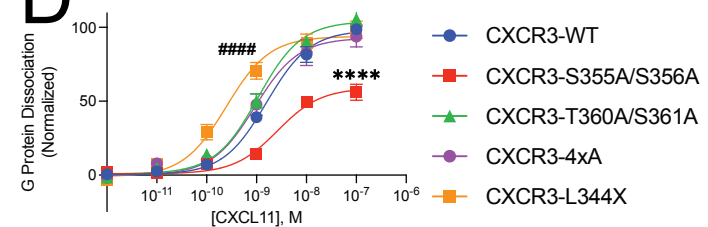
C



A

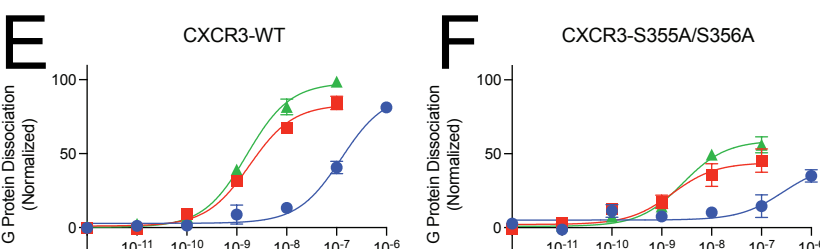


D

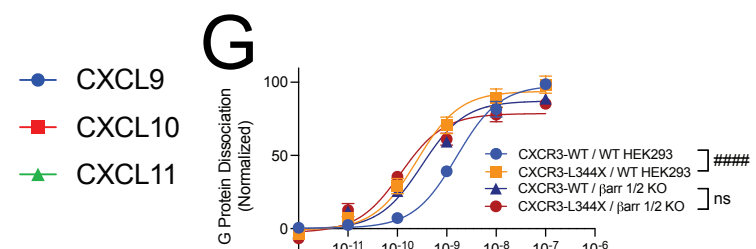


E

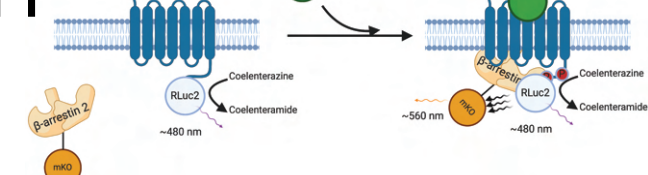
F



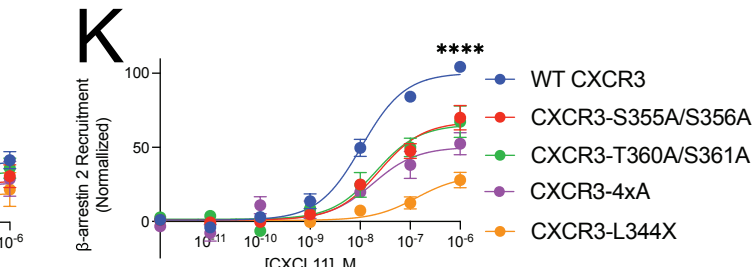
G



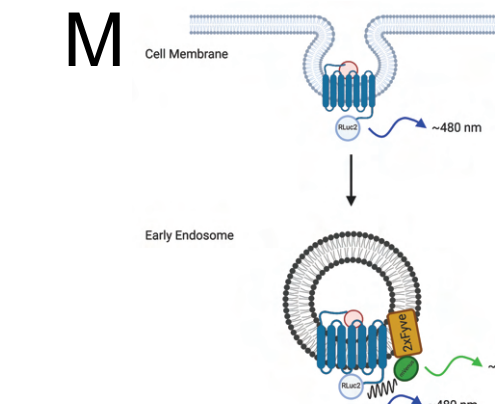
H



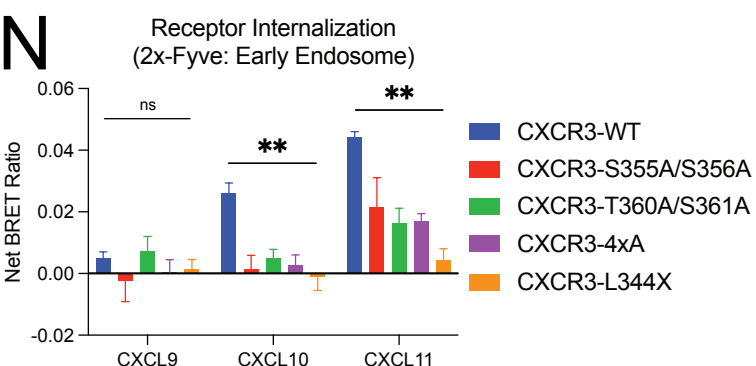
K



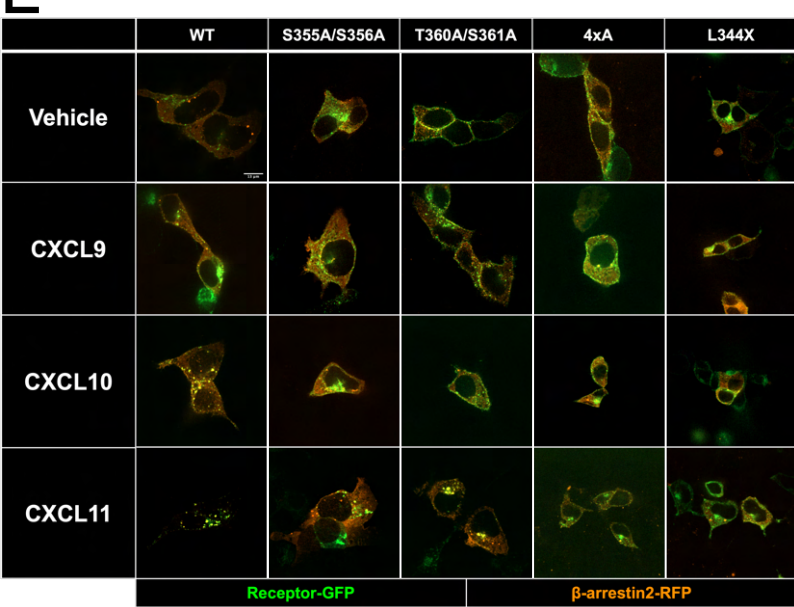
M

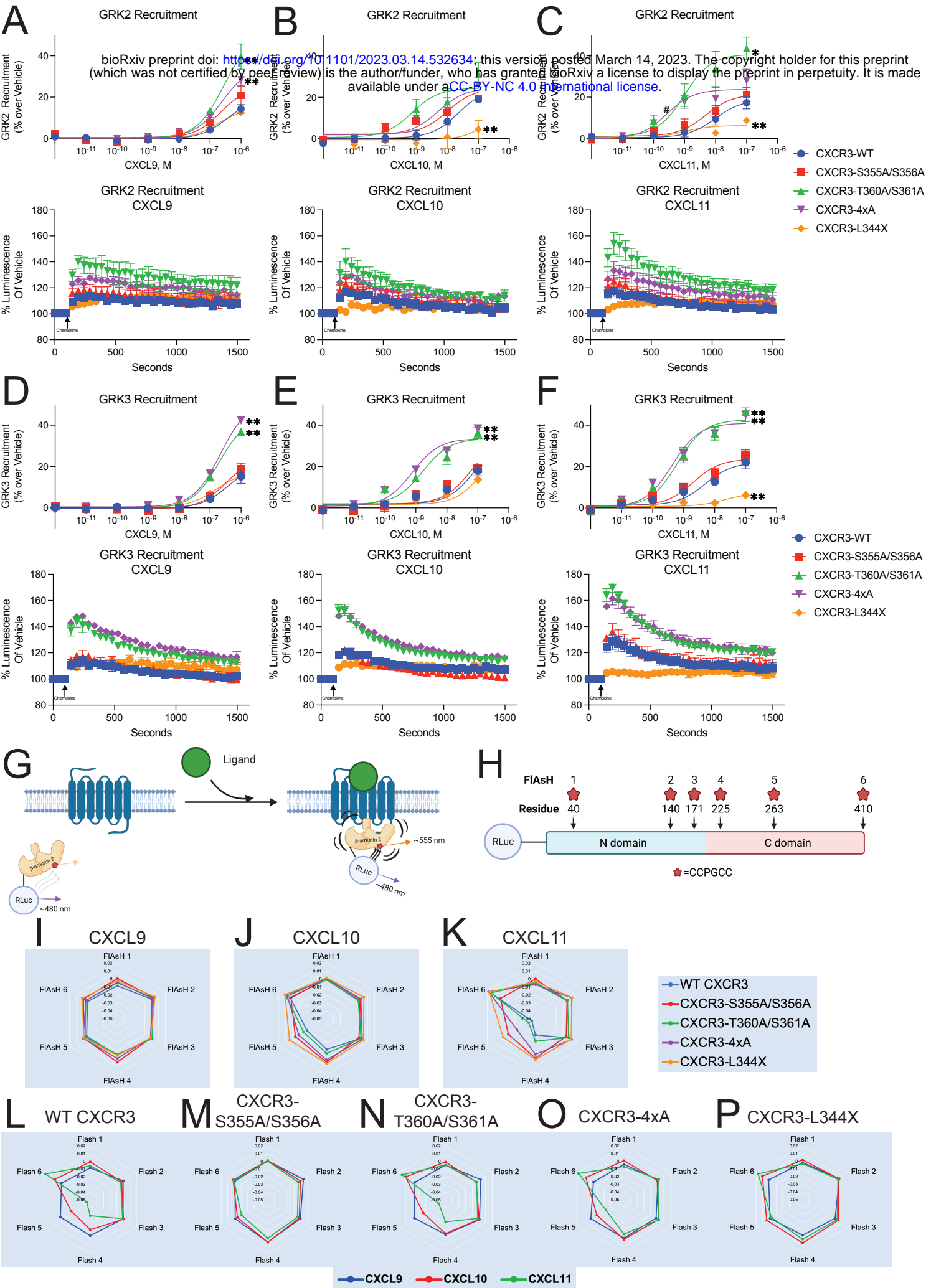


N



L

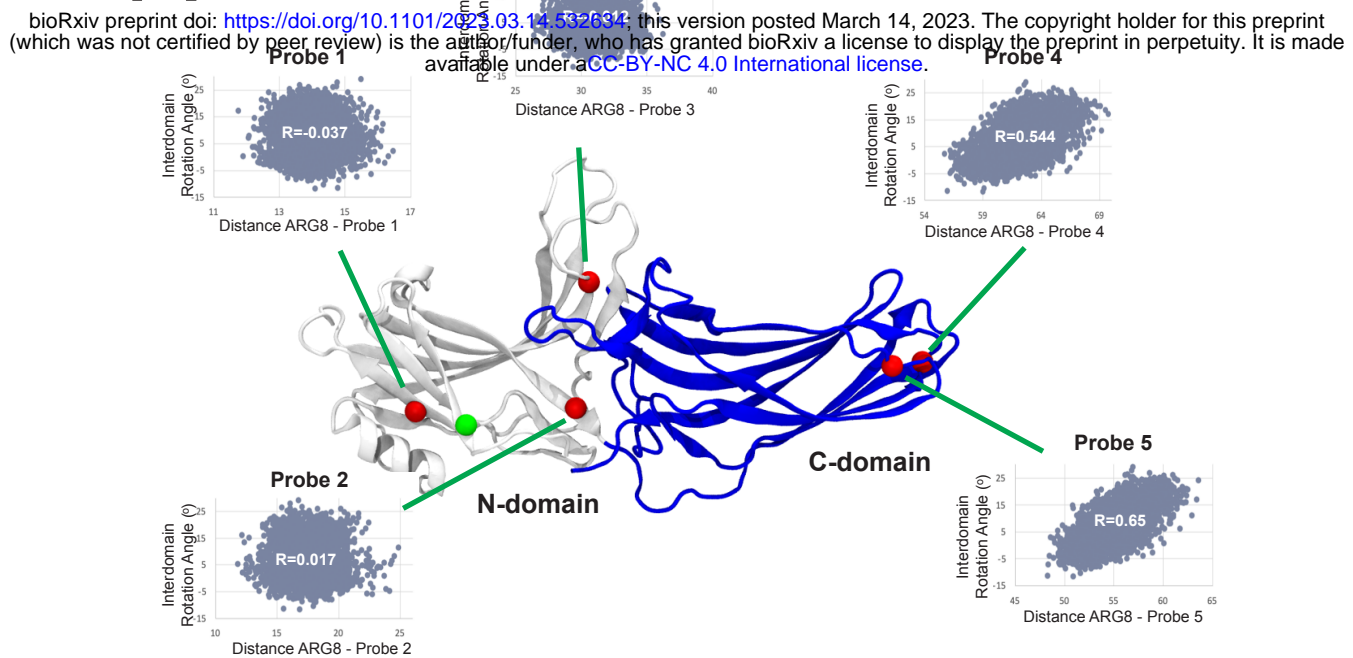


**FIGURE 3**

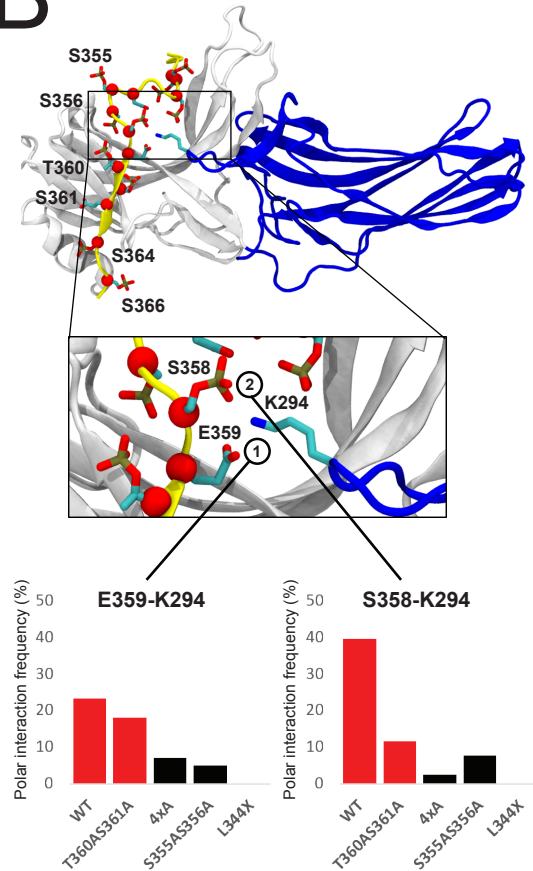
# FIGURE 4

Figure 4

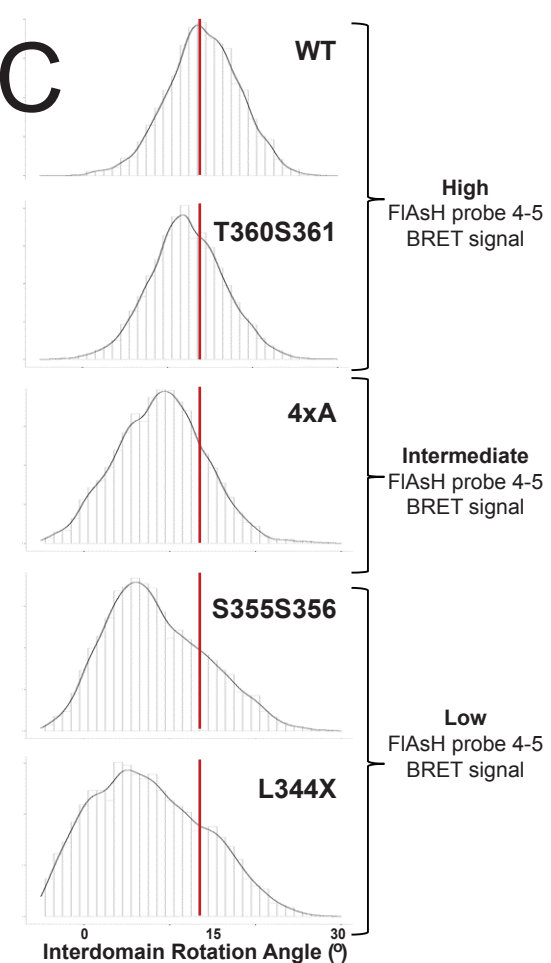
**A**

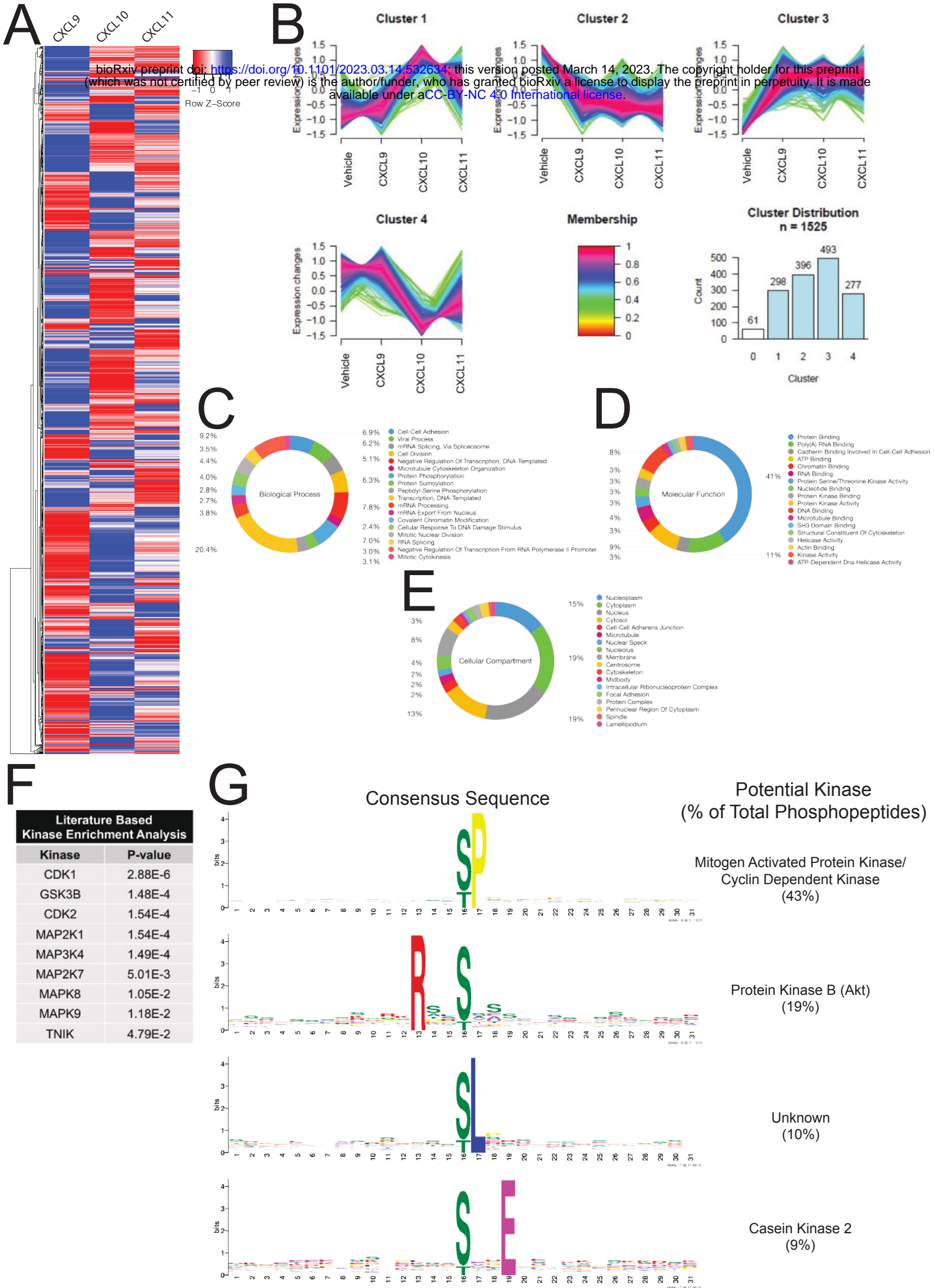


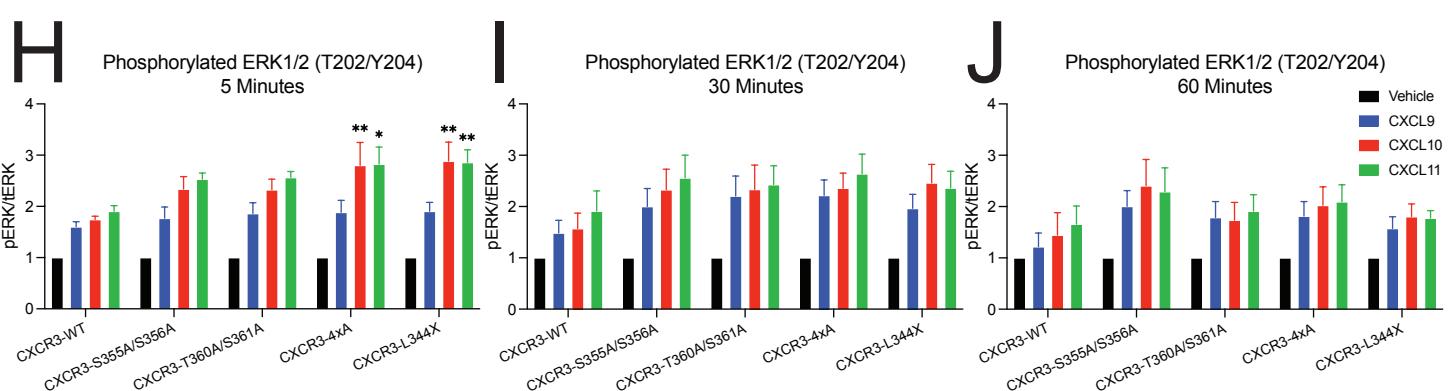
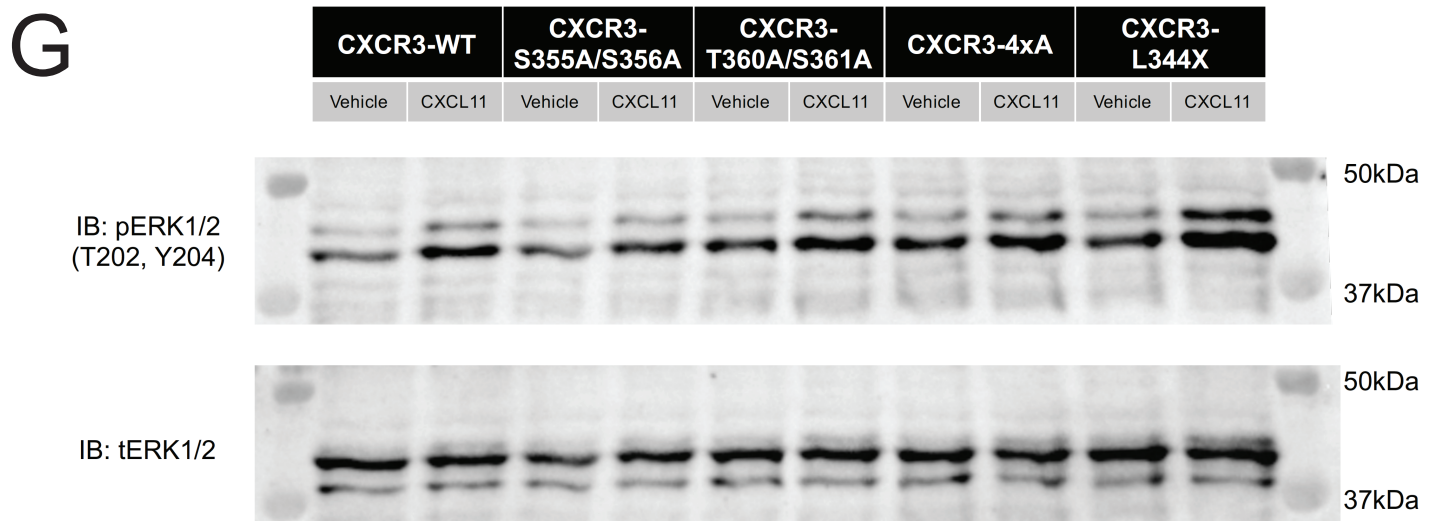
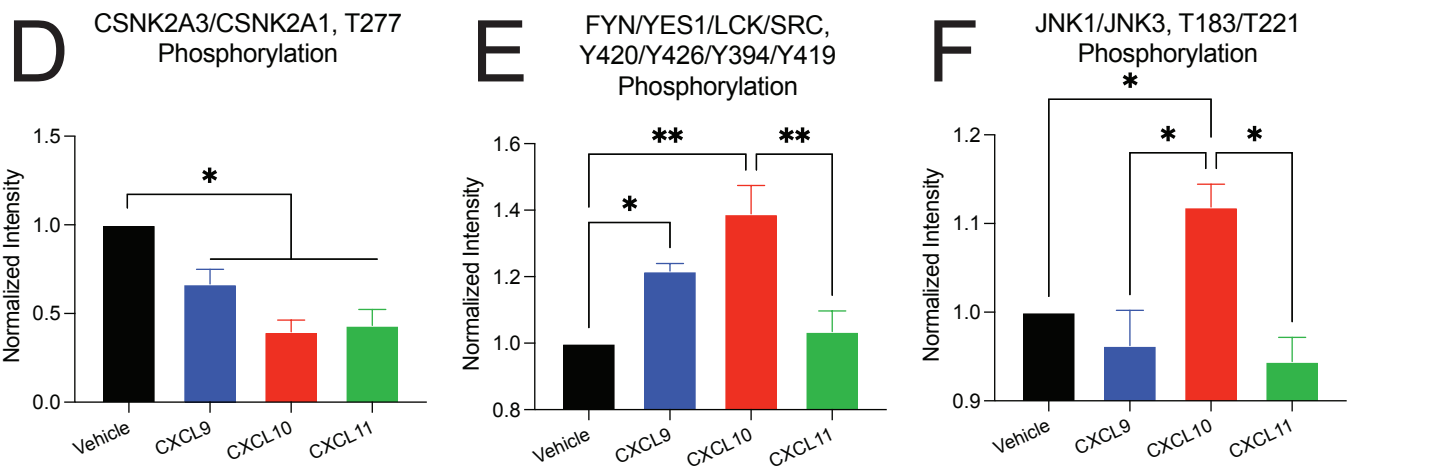
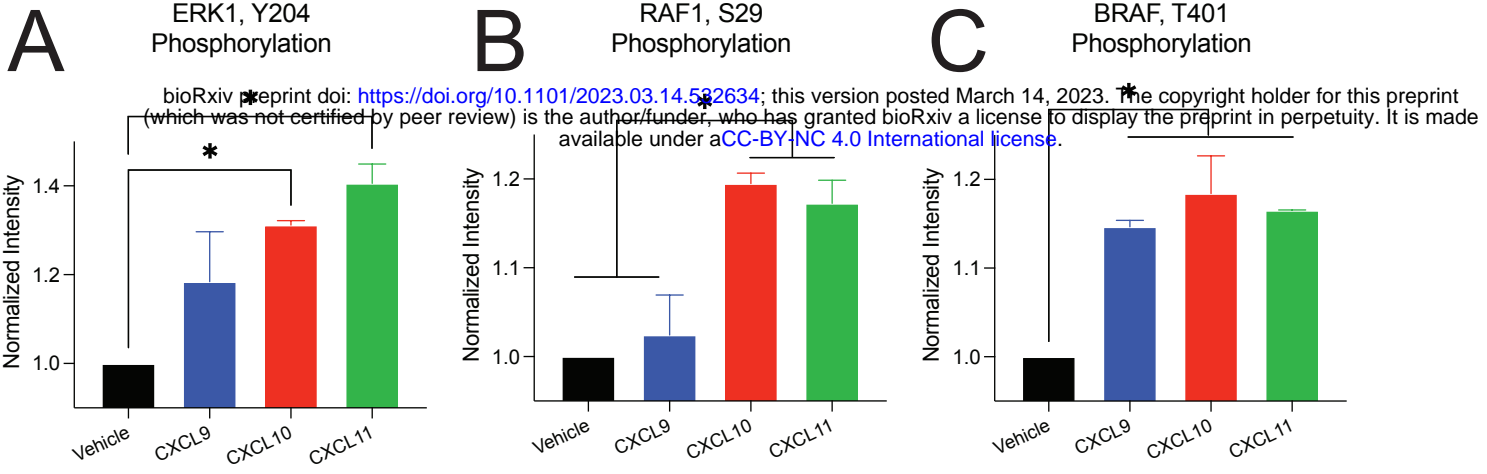
**B**



**C**



**FIGURE 5**

**FIGURE 6**

**FIGURE 7**